OPEN ACCESS
IOP Publishing
Journal of Physics D: Applied Physics
J. Phys. D: Appl. Phys. **58** (2025) 125302 (21pp)
https://doi.org/10.1088/1361-6463/ada44d

Eumelanin & keratin sourced from waste: unraveling criss-cross functionalities for green electronic applications

Marianna Ambrico[1,*], Sara Mattiello[2], Albertus Bernardus Mostert[3], Jun Wei Phua[4], Domenico Aceto[1], Paolo F Ambrico[1], Alessandro Guzzini[2], Angelo De Stradis[5], Federico Liuzzi[6], Carlo Santulli[2], Giulio Lupidi[7], Alessandra Del Giudice[8] and Roberto Gunnella[2]

[1] CNR-Institute for Plasma Science and Technology, Bari Branch, Via Amendola 122/D, I-70125 Bari, Italy
[2] School of Science and Technology University of Camerino, Via Madonna delle Carceri 9, I-62032 Camerino, MC, Italy
[3] Centre for Integrative Semiconductor Materials, Department of Physics, Swansea University Bay Campus, Fabian Way, Swansea SA1 8EN, United Kingdom
[4] INSECTTA Pte. Ltd, 8 Cleantech Loop, Singapore 637145, Singapore
[5] CNR-Institute for Sustainable Plant Protection, Bari Branch, Via Amendola 165/A, I-70126 Bari, Italy
[6] ENEA-Centro Ricerche Trisaia, S.S. 106 Ionica 301-75026 Rotondella, MT, Italy
[7] School of Pharmaceutical Sciences and Health Products, University of Camerino, Via Madonna delle Carceri 9 I-62032 Camerino, MC, Italy
[8] Department of Chemistry, Università 'La Sapienza' di Roma, Piazzale Aldo Moro, 5, 00185 Rome, Italy

E-mail: marianna.ambrico@istp.cnr.it

Received 17 October 2024, revised 5 December 2024
Accepted for publication 30 December 2024
Published 23 January 2025

Abstract

In the framework of the Circular Economy this study provides a detailed analysis of water-based suspensions of two biopolymers derived by sustainable processes: eumelanin from insect farming and keratin from chicken feathers. The latter material was obtained via two different extraction procedures. Colloidal-like suspensions were produced in water either as a single component system or a mixture of both in selected ratios, taking advantage of their high solubility. The suspensions were examined using a comprehensive set of chemical, structural and dielectric techniques to gather information on their properties. Small-Angle x-ray Scattering results provided insights into the elemental polymer sections within the suspension, while Transmission Electron Microscopy images indicate that keratin is the component driving the shape of the aggregation structure in a colloidal environment, and, in some cases, eumelanin internalization. Furthermore, the co-presence of both polymers in water determines the aggregation dimensions and shapes. The discussion focuses on the influence of the aggregation on the dielectric proper-ties by comparing the former to the AC dynamic response returned by

* Author to whom any correspondence should be addressed.

Broadband Dielectric Spectroscopy (BDS). Within the BDS framework various items are highlighted including dielectric relaxations, screening effects, counterion condensation and ionic charge transport. The results shown in this work let to foresee the adoption of water or biofriendly aqueous BSF-EuM:Keratin suspensions in the production of devices and sensors with low environmental impact.

Supplementary material for this article is available online

Keywords: circular economy, organic waste, eumelanin, keratin, TEM, SAXS, dielectric spectroscopy

1. Introduction

A key objective of the Circular Economic (CE) is 'to minimize waste and promote a sustainable use of natural resources, through smarter product design, longer use, recycling and more, as well as regenerate nature' [1]. In this framework, one of the CE challenge is to reduce the waste production and/or the adoption of effective solutions in waste management.

One example of applying CE thinking to a major source of waste is to the organic fraction from municipal waste. Based on the most recent 2022 European Compost Network (ECN) report, '[2] an estimated 71 million metric tons per annum (tpa) of separately collected biowaste were treated through composting and anaerobic digestion (60 million tpa in the EU27 and 11 million in CH, NO and UK)'. These estimates included both municipal and commercial/industrial biowastes. Composting accounted for 42 million tpa (59%), while anaerobic digestion (AD) accounted for 29 million tpa (41%) [2].

A parallel problem has also emerged due to the increase in the use of electronics. The large variety of electronic devices, from the simplest ones such as disposable sensors, to the most complex ones such as batteries, PCs, mobile phones etc are all rapidly subjected to hardware updates. As a result, a significant amount of electronic waste (e-waste) is produced (>45 megatons per year), adding strain to the environment [3, 4]. Therefore, e-waste management constitutes a new challenge for a CE approach. One partial solution can be found in the introduction of biodegradable electronics, whose products coming from decomposition or disintegration will lessen the impact on the environment [3].

However, other major activities produce organic waste, for which effective CE solutions are still to be found. Among the others, wool and poultry industries, which contribute large amounts of waste [5].

Recently, two categories of organic waste have become an unexpected resource that could potentially address the e-waste and wool/poultry farming waste problems: eumelanin, obtained via processing of black soldier fly larvae shed skins (BSF-EuM) and keratin obtained from wool and feathers via industrial processes. This has been the result of companies and start-ups investing in innovative processes trying to push them more and more towards low or zero environmental impact. A specific aim is the extraction of biomaterials with unique functionalities, making them spendable on the market in diverse areas of manufacturing, packaging, environmental technologies, medicine, and agriculture [6].

These two classes of materials, eumelanin and keratin, are the focus of this work, and are in general of great interest as many research groups worldwide have investigated them for their useful properties [7–19].

The eumelanin materials can be classified into three main compounds that are associated to the more traditional, nitrogen containing materials, with the primary compound called eumelanin (commonly termed melanin) and is a black-brown pigment derived at least in part from the oxidative polymerization of L-dopa via 5,6-dihydroxyindole intermediates; the second main compound is pheoeumelanin, a yellow-to-reddish brown sulfur containing pigment derived from the oxidation of cysteinyldopa precursors via benzothiazine and benzothiazole intermediates. The third main compound is neuroeumelanin, found in the substantia nigra of the brain stem and is a dark pigment produced within neurons by the oxidation of dopamine and other catecholamine precursors that has been shown to contain a pheoeumelanin core and a eumelanin outer shell [20–22].

Eumelanin, the melanin investigated herein, is of technological interest due to its properties and demonstration of use in devices. Properties include broad band optical absorbance [23–25], metal ion chelation [26], paramagnetism [27], radiation protection [28, 29], and humidity dependent conductivity [25, 30–32], to name a few. For devices, several examples include electrochemical transistors [31, 33, 34], energy storage [35–38], memory [39, 40], optoelectronic skins [41], phototransistors [42], coloring films [43], and sensors [7, 44–47]. Eumelanin has the additional advantage of demonstrating biodegradability with reduced phytotoxic effects, thus paving the way for its use as a potential green electronics material [48].

Keratin represents the most abundant structural protein in epithelial cells and, together with collagen, the most important biopolymer in animals [49]. Given its biological origin, it is remarkable to see its toughness and wide range of functions. For instance, scales provide body armor, horns are used for combat, hagfish slime acts as a defense against predators, nails and claws enhance prehension, and hair and fur protect against environmental elements. These inspiring examples can offer valuable insights for designing new structural and functional

materials. Different forms of keratin can be obtained with different phases of purification, appropriately modulated and depending on the origin (e.g. wool or feathers), yielding differentiation in structure, which allows for example, the production from membranes to gels [10, 13]. The various properties of these keratin substances make them interesting from an application point of view for microelectronics, applied medicine, and energy storage [13, 14, 50].

Eumelanin contains both amino and catechol groups that are well known for metal ion chelation [51], which we anticipate being an anchoring mechanism for eumelanin internalization into keratin biopolymers, as suggested by the removal of eumelanin from melanocytes into keratinocytes [52]. Thus, we envisage new multifunctional materials of eumelanin/keratin for exploitation.

With the above background, we were stimulated towards a deeper understanding of the chemical, structural and electrical transport properties of eumelanin-keratin materials. Especially given that the properties of the elicited biopolymers and their combination can significantly alter their properties and enabling interfacing with both biological and inorganic systems. For melanic materials, the advantage they confer is they can carry both ionic and electronic current compatible with the demands of bio-electronic devices [53]. The multiplicity of final morphological structures of keratin, together with their strength and adhesiveness makes them suitable for supporting appropriate functionalization steps.

Notably, the high solubility/dispersibility in water for both materials allow studying them in a peculiar environment at a neutral pH, without altering the chemistry of either biopolymer. Also, this peculiarity makes them of particularly interest in transient electronic devices and specifically in those adopted in biology or medicine, where sensors are mainly working once in water-exposed conditions, and where the biodegradability and high performance are requirements [54].

An additional side benefit is that exploring the electrical transport properties in an only water-based suspension, one can investigate and isolate redox processes that is between H_2O and the unaltered chemical structure of these materials, whether a single component or a mixture.

With the above in mind, this work will develop through the investigation firstly water-based suspensions of each component, and then their mixtures. We will first present the chemical and structural aspects of these systems, with experimental data from FTIR on powders then from TEM and SAXS. From this data set we will infer the resulting functionality and modification of the mixtures from the baseline materials.

Once the chemical and structural data has been presented, we will show in the second part of this work the electrical responses via broadband dielectric spectroscopy (BDS) of these materials in water suspensions. The resemblance between these suspensions (both single-component and mixed) and those involving hydrated proteins (as discussed by the first relevant paper of Schwan and recently by Nakanishi [55, 56]) prompts us to focus on analyzing the BDS spectra. In our study, we will extensively analyze the BDS data within the framework of the Havriliak-Negami (HN) dielectric modeling. This approach is like a recent study we have conducted on solid state eumelanin samples [57].

Insights gained will then be correlated back to the chemical and structural work.

2. Materials and methods

2.1. BSF-EuMelanin and Keratin extraction methods

The eumelanin investigated in this paper is extracted by the start-up Insectta Pte. Ltd from the pupal exuviae of the black soldier fly larvae. This company occupies a circular economic position within Singapore, in which the flies are used to valorize food waste, and the black soldier fly eumelanin (BSF-EuMelanin, from now on labeled as BSF-EuM for sake of conciness, whenever needed) is a value-added product currently co-extracted during the process of chitin production. The production cost is therefore low, while the yield is approximately 1% by weight from pupal exuviae. Thus, the BSF-EuM appears to be a competitive product, critically being based upon a circular economic approach. The expectation is that price will continue to decrease and volume increase as the product becomes more widely recognizable, and applications are found for it.

BSF-EuM was isolated from the black soldier fly (Hermetia illucens) according to a patented protocol released by Insectta [58]. The process in brief is as follows: Hermetia Illucens pupal exuviae were minced into approximately 0.5 mm pieces using a blender (Robot Coupe Blixer 4, France). The pupal exuviae were then demineralized with 10% (w/w) lactic acid at room temperature for 3 h. To reduce protein contamination in the eumelanin fraction, deproteination of the pupal exuviae was performed with 1 M NaOH for 3 h at 50 °C. Subsequently, eumelanin was liberated by heating the mixture with 3 M NaOH, for 2 h at 90 °C. Thorough washing of the mixture was performed in between steps. The eumelanin-containing supernatant was filtered through a 500 mm mesh nylon cloth, with the eumelanin fraction precipitated with the addition of 37% (v/v) HCl of a series of proprietary steps. The procedure is then concluded with lyophilization to obtain salt-free, water-soluble, sub-micrometres particles of BSF-EuM.

In this work two types of keratins are investigated. The first type of keratin used in this work is extracted from organic waste feathers samples, but adopting the steam explosion extraction technique, which we labeled as KerST. In this process the biomass is treated with hot steam (180 °C–240 °C) under pressure (1–3.5 MPa) followed by an explosive decompression, resulting in a breakage of the rigid structure of the fibers [59, 60]. Feathers for the process were prepared as follows: a first wash with cold water and common soap followed by drying at 60 °C in a forced-air oven. The second wash is then with ethanol at 50 °C for 2 h to remove surface fats and waxes. The defatted feathers were then removed from the ethanol solvent and ethanol residue removed after incubation for 3 h in a forced-air oven at 60 °C. The feathers were then soaked in demineralized water, at a ratio of 1:1 feather to water. This mixture is then pretreated using steam explosion using an ENEA 10 l Staketech batch digester at 200 °C for 10 min

Table 1. List of mixtures investigated in this study. * Filtered by a 0.45 μm membrane before the measurement.

Suspensions	Mel:Ker	Items code	SAXS (mg ml^{-1})	BDS/TEM (mg ml^{-1})
BSF-EuMF*	1:0	S0F	—	10
BSF-EuMUF	1:0	S0UF	4.0	10
KerST	0:1	S10	17.5	10
KerBS	0:1	S20	7.5	10
BSF-EuM:KerST 15*	1:4	S15	10	10
BSF-EuM: KerST 16*	1:9	S16	—	10
BSF-EuM: KerST 17*	4:1	S17	—	10
BSF-EuM : KerST 18*	9:1	S18	—	10
BSF-EuM :KerBS 21*	1:4	S21	10	10
BSF-EuM :KerBS 22*	1:9	S22	—	10
BSF-EuM :KerBS 23*	4:1	S23	—	10
BSF-EuM :KerBS 24*	9:1	S24	—	10

under a pressure of 15 bar. After 10 min of each pre-treatment with saturated steam, the biomass was rapidly transitioned to atmospheric pressure by opening an electronic valve, promoting further breakdown. The impregnation process favors the deconstruction of the biomass within the reactor [61]. The steam explosion process was carried out in duplicate and from the process we obtained keratin in water solution at a concentration of 45 mg ml^{-1}. To obtain powder samples useful for measurement, KerST was subjected to a lyophilization process. This process removes the water by freezing the material, then lowering the pressure and applying heat, causing the frozen water to sublimate directly from solid to vapor [62]. For lyophilization we employed a FreeZone Freeze Dryer (LABCONCO), subjecting the samples to 0.02 mbar in vacuum at 20 °C for about 5 d.

The second keratin system was extracted from the same organic waste feathers (KerBS) as the KerST using the chemical process, as described in Mattiello *et al* [63], consisting of a metabisulfite extraction method. This process was selected as it provides sufficient persistence of the secondary structure of the protein. In addition, the procedure is effective, easily applicable to the raw material, requires lower amounts of chemicals and has a lower toxicity compared to other methods such as the mercaptoethanol method [64, 65].

2.2. Suspensions preparation

The solutions and concentration shown in this work are shown in table 1. For SAXS measurements the concentration in single component suspension was regulated to reduce the interactions between the chains and study the fine structure. In mixed suspensions the final concentration was still 10 mg ml^{-1} keeping the same mass ratio and concentration adopted for BDS/TEM measures. The measurement was focused on the 1:4 mass ratio in both keratin types.

In BDS/TEM measurements the suspensions were made by dissolving the powders of the biopolymers, whether single or mixed, in deionized water (H2O conductivity $\sigma = 1.0$ μS cm^{-1}). The total concentration of the biopolymer was 10 mg ml^{-1}, with the ratio between BSF-EuM and Keratin varied by mass.

In all the characterizations, the various suspensions were filtered by a 0.45 μm filter membranes, a procedure that enabled the selection of particles with similar dimensions and, in BSF-EuM the removal of residual protein in BSF-Eumel.

2.3. Transmission electron microscopy (TEM)

For TEM analysis, a drop (20 μl) of a solution was applied to a carbon-coated copper/rhodium grid (400 mesh) (TAAB Laboratories Equipment Ltd, Aldermaston, Berks, ENGLAND). The coated grid was floated for 2 min on the drop, rinsed with 200 μl of double distilled water and then stained by a negative staining solution (200 μl of 0.5% w/v UA-Zero EM stain, Agar-Scientific Ltd, Stansted, UK). After draining off the excess staining solution by means of dabbing it with filter paper, the specimen was then transferred to the electron microscope for examination, using a Philips Morgagni 282D transmission electron microscope, operating at 80 kV. Electron micrographs of negatively stained samples were photographed on Kodak electron microscope film 4489 (Kodak Company, New York, USA). The negative staining procedure is employed to take advantage of increased electron scattering from higher density materials. Consequently, electrons being scattered from the negative staining solution exhibit brighter signals in the resulting images. In non-homogenous items, the final images is shown in grayscale; the bright region means 100% materials, the black absence of material.

2.4. Fourier transform infrared spectroscopy (FT-IR)

FT-IR spectra were recorded from 4000 to 600 cm^{-1} with a PerkinElmer Spectrum 100 FT-IR instrument (Waltham, MA, USA) by total reflectance utilizing a CdSe crystal. The FT-IR spectra were collected on KerBS and BSF-EuM in powder form.

2.5. Small-angle x-ray scattering (SAXS)

SAXS experiments were performed using a Xeuss 2.0 Q Xoom system (Xenocs SA, Grenoble, France) equipped with a microfocus Genix 3D x-ray Cu source ($\lambda = 0.1542$ nm) and a

two-dimensional Pilatus3 R 300 K detector placed at variable distance from the sample (Dectris Ltd, Baden, Switzerland). Measurements were made on liquid solutions obtained by dissolving powder samples in distilled water (DI) at different concentrations as listed in table 1.

The samples were loaded into disposable borosilicate capillaries with nominal thick-ness 1.5 mm and sealed with hot glue. Two capillaries, one loaded with the deionized water used as dispersant and an empty one, were used for background subtraction.

The measurements were performed at room temperature and at reduced pressure (∼0.2 mbar), with two different sample-detector distances to access a scattering vector modulus (q) range between 0.045 and 13 nm^{-1}, where $q = \frac{4\pi \sin(\theta)}{\lambda}$, 2θ is the scattering angle and λ is the x-ray wavelength of light. The two-dimensional scattering patterns were subtracted for the 'dark' counts, and then masked, azimuthally averaged, and normalized for transmitted beam intensity, exposure time, and subtended solid angle per pixel, by using the FoxTrot software developed at SOLEIL. The one-dimensional intensity vs. q profiles were subtracted for the contributions of the solvent and empty capillary and reported in intensity units of macroscopic scattering cross-section (cm^{-1}) by dividing by the capillary thickness estimated from the alignment scans. Pair distance distributions were obtained by indirect Fourier inversion of the $I(q)$ profiles, or $I(q)\cdot q$ in case of the cross-section of elongated objects. These distributions were obtained with the software BayesApp [66]. Model intensities to help data interpretation were calculated using the software SASfit [67].

2.6. Electrical measurements configuration and experimental apparatus

The electrical measurements of the suspensions were done by using a disposable standard 8 well arrays (Applied Biophysics, maximum volume well 600 μl, figure 1) provided with interdigitated Au electrodes (IDE) at the bottom side. The IDE structure consists of a comb structure composed of nine couples of Au electrode fingers, 0.8 cm long, placed at 50 μm.

The sampling of the suspension was kept constant by using only 200 μl, whereas the IDE configuration ensured a consistent electrode geometry, thus eliminating variation from geometrical effects. The electrical data of the suspensions were measured using Electrical Impedance Spectroscopy (EIS), where the complex impedance of the suspension Z is obtained from scanning several frequencies of sinusoidal, alternating current-voltage measurements.

The EIS measurements were obtained by a NOVOCONTROL Impedance Analyzer. The AC voltage signal amplitude (V_{AC}) was fixed at 300.0 mV, DC offset was 0.0 V, and the frequency (f) range scan was between 0.1 Hz to 10.0 MHz, 8 pts/decade, with a total of 56 points and a recording time of around three minutes.

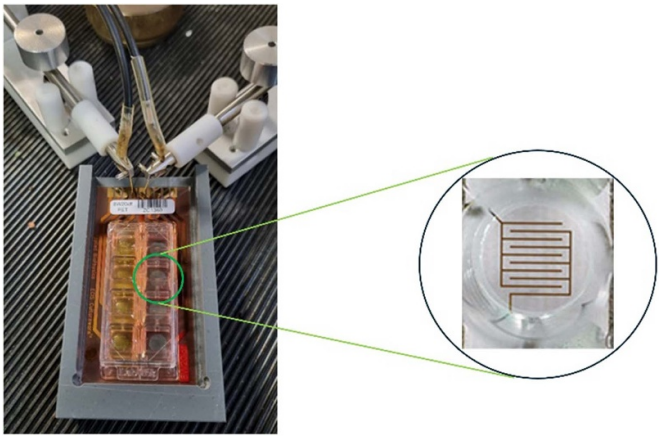

Figure 1. Representative disposable 8 well arrays provided by IDE at the bottom side (left, Applied BioPhysics) and probe connection to the measurement apparatus adopted for the electrical measurements on suspensions. The enlarged view of the IDE on the bottom of the well is shown on the right.

2.7. Electric data analysis and modeling

The EIS data were analyzed within the broadband dielectric spectroscopy (BDS) approach, utilizing two representations: the first is the complex dielectric permittivity ε^* spectra; the second is the complex AC conductivity spectra, σ^*.

The permittivity ε^* is related to the real (ε') and imaginary (ε'') components as:

$$\varepsilon^* = \varepsilon' - j\varepsilon''. \tag{1}$$

Each component is calculated from the complex impedance by [56, 68] by the following equation

$$\varepsilon' = \frac{-\mathrm{Im}\ [Z]}{2\pi f |Z|^2 C_0}; \text{and } \varepsilon'' = \frac{-\mathrm{Re}\ [Z]}{2\pi f |Z|^2 C_0} \tag{2}$$

with C_0 representing the equivalent vacuum cell capacitance, $|Z|$ the modulus of the impedance Z and f the frequency. In the present case, since it is difficult to estimate the geometrical parameters, we obtained C_0 by directly measuring the impedance vs. frequency on the empty cell and taking the value at the highest frequency, which is related to the dielectric constant and geometrical parameter of the cell [69]. We obtained a value of $C_0 = (1.0 \pm 0.1) \times 10^{-13}$ F cm^{-1}.

Additionally, the loss factor $\tan\delta$ is derived via:

$$\tan\delta = \frac{\varepsilon''}{\varepsilon'}. \tag{3}$$

We adopt the Trukhan model to estimate the diffusion coefficient D_{ion} of free ionic charge carriers where [57, 70]:

$$D_{ion} = \frac{\omega_{max} L^2}{9 \times 32 \left(\tan\delta_{max}\right)^3} \tag{4}$$

that has been rescaled with respect two known parameters, i.e. the number of finger couples (9) and finger distance

($L = 50\ \mu$m). The 'max' subscription indicates the radial frequency position and corresponding value of the maximum of the loss factor

The free ionic concentration n is then determined from the Nerst equation by

$$n = \frac{\sigma'_{DC}}{e^2}\frac{k_B T}{D} \tag{5}$$

where e is the fundamental charge and $\sigma'_{\mathrm{DC}}$is the real part of the conductivity at $\omega_{\max}$, i.e. the conductivity corresponding to the plateau value in the real AC conductivity spectrum, $k_B T$ is as normal Boltzmann's constant and temperature multiplied, which for room temperature and our measurements is 0.025 eV. Also, the Debye lengths are calculated as:

$$L_D = \frac{L}{8(\tan\delta_{\max})^2}. \tag{6}$$

Since the as calculated ε' spectra also includes the DC conductivity contribution, it is useful to remove it by representing a particular ε' derivative (Kramers-Kronig relationship) with respect to lnω where ($\omega = 2\pi$f) is the radial frequency [56, 71]:

$$D_{\ln\omega}\varepsilon'(\omega) = -\frac{\pi}{2}\frac{\partial\varepsilon'}{\partial\ln\omega} \approx \varepsilon''_{\mathrm{rel}}. \tag{7}$$

Here we adopt the *'D'* notation for the derivative. $\varepsilon''_{\mathrm{rel}}$ is the dissipation of the complex dielectric function, but which excludes the conductive components of the dissipation, leaving only the polarizing components. This feature enables the better resolution of polarization relaxation peaks, especially peaks at lower frequencies assigned to α and β relaxations [71, 72]. This is justified since we are examining the AC response of protein-derived systems [56].

Considering the equivalence of the derivative in expr. 7 with $\varepsilon''_{\mathrm{rel}}$, it comes out that the relaxation processes will be featured by the same parameters as $\varepsilon'_{\mathrm{rel}}$. Therefore, we can apply the Havriliak-Negami (HN) formalism, which is used to model relaxation peaks, but without the conductivity term [56, 71]. This means that we examine the derivative of the real part of the dielectric permittivity via:

$$D_{\ln\omega}\varepsilon'(\omega) = \sum_{i=1}^{K}\left[\frac{\Delta\varepsilon_i}{\left(1+(j\omega\tau_{HNi}^{a_i})^{b_i}\right)}\right]. \tag{8}$$

The superposition of up to three ($K = 3$) dielectric relaxation functions enabled to achieve the best fit of the spectra. Each HN function is featured by a relaxation time distribution peak at a specific relaxation time (τ_{HNi}), with characteristic parameters $\Delta\varepsilon_i$, termed as the dielectric strength and coefficients a_i and b_i. The former coefficient is assigned to the broadening and the latter to the symmetry of the time relaxation peak [73–75].

The frequency of the peak $f_{\mathrm{MAX,HNi}}$ for each relaxation (α, β, EP, see below for further definition) is determined from the τ_{HNi} values by using [76]:

$$f_{\mathrm{MAX,HNi}} = \frac{\omega_{\mathrm{MAX,HNi}}}{2\pi} = \left(\frac{\sin\left(\frac{\pi a_{\mathrm{HNi}}}{2(b_{\mathrm{HNi}}+1)}\right)}{\sin\left(\frac{\pi b a_{\mathrm{HN}}}{2(b_{\mathrm{HNi}}+1)}\right)}\right)^{a^{-1}} \tau_{\mathrm{HNi}}^{-1},$$

$$\mathrm{HNi} = \alpha, \beta, EP\,. \tag{9}$$

From now on we will use $f_{\alpha/\beta/\mathrm{EP}}$ and $\omega_{\alpha/\beta/\mathrm{EP}}$ referring to the values determined via expr. 9.

A consolidated picture considers the dielectric relaxations observed in polyelectrolyte in aqueous solutions as due to counterion polarizability, balancing the ionic groups in the polymer backbone [77]. The peculiar chemical structure of eumelanin and keratin let to assigned both to the class of (poly)electrolyte [17, 78] where proton ions (H_3O^+) acts as the counterions.

Within a polyelectrolyte system a phenomenon of counter ion condensation in water is highly probable. This situation is when the charge density of a linear polyelectrolyte chains exceeds a critical value that is then neutralized by counterions in solution; 'Free' counterions 'condense' in the vicinity of the chain such that the Coulomb repulsion energy of two adjacent charged groups on the chain decreases below kT [79].

This condensation condition is reached when the separation, d, of monovalent charges along the polymer chain is less than the Bjerrum length l_B where $l_B = \mathrm{e}^2/(4\pi\varepsilon_r\varepsilon_0 \mathrm{kT})$. This condition is generally satisfied for polyelectrolytes in water since $\varepsilon_r(H_2O) = 80$, which yields an $l_B = 7$ Å while $d < 7$ Å [77].

This condensation manifests itself in the dielectric response as a feature at low frequency f_α (α -relaxation) with polarization along the longitudinal direction of the polymeric chain. Whereas the β-relaxation frequency, f_β, represents the free counterions still available and is seen at higher frequencies and polarization along the radial along the radial direction [77].

Given that these frequencies relate also to the linear l_α and radial l_β dimension of the polymeric aggregates, one can determine these effective lengths via the diffusion coefficients of the condensed $D_{\mathrm{ion},\alpha}$ and free counterions $D_{\mathrm{ion},\beta}$ [77, 80–82]:

$$f_{\mathrm{MAX}(\alpha/\beta)} \sim \frac{6D_{\mathrm{ion}(\alpha/\beta)}}{l^2_{\alpha/\beta}} \quad \text{and} \quad \omega_{\mathrm{MAX}(\alpha/\beta)} = 2\pi f_{\mathrm{MAX}(\alpha/\beta)} \tag{10}$$

where $D_{\mathrm{ion}_{(\alpha/\beta)}}$ are the Nerst diffusion coefficient (expr. 4) corresponding to the conductivity values at f_α and f_β. As a first approximation we will use the free ionic charge density n as calculated via the Trukhan Model in expr. 5 to estimate the corresponding counterion density either in the calculation of both D_{ion_α} or D_{ion_β}.

3. Results and discussion

3.1. Transmission microscopy results

The BSF-EuM morphology in the filtered suspension (BSF-EuMF) as observed by TEM (figure 2) was characterized by

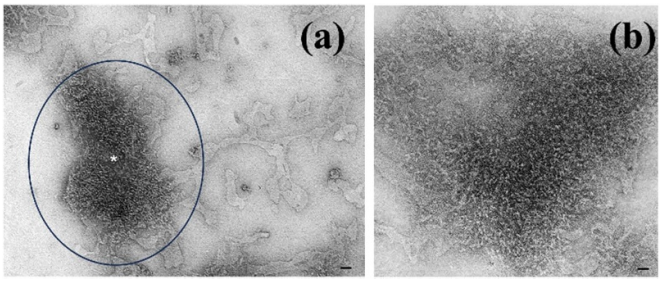

Figure 2. (a) TEM images of the BSF-EuMF structure; magnification 30.000X, bar = 100 nm. The bright region refers to high particle density continuously dispersed and the gray/black zone refers to a low particle density region both assuming a sheet like structure (b) Magnified image of the region indicated via the asterisk and circle, (magnification 150.000X, bar = 30nm), evidencing a low-density region of the sheet constituted by a discrete aggregation of nanoparticles ø = 5 nm.

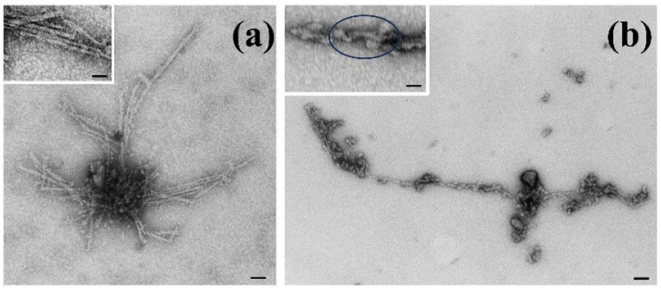

Figure 3. TEM images of the (a) KerST, left and (b) KerBS, right structure; in both cases the magnification 80.000X, bar = 40 nm and for the inset 150.000X, bar = 25 nm. In (a) KerST: Star-like aggregation and tubular filamentary structure (the inset in figure 3(a) is a magnification of the tubular structure). In (b) KerBS: Linear aggregation in a bent-like structure; the inset displays a magnified view highlighting the presence of a helix- like bent structure.

a non-homogeneous distribution of submicrometric colloidal particles represented by the bright region of figure 2(a) that contours, and a high density of small colloidal particle aggregation represented by the gray/black region (on the left side of figure 2(a) and magnified in figure 2(b)). The estimated dimension of the particles has been measured between 4 and 10 nm in size (modal value ∼7 nm) in agreement with other previous observations [9].

The KerST and KerBS structures (figures 3(a) and (b) respectively) resulted immersed in a colloidal suspension, (bright region) made up of dispersed particles. Notably, their size has been found non uniform in KerST and highly homogenous in KerBS. Moreover, KerST displayed starlight aggregation featured by tubular filamentary structure (see inset in figure 3(a)), whereas KerBS displayed a linear belt structure. Furthermore, the magnification of the KerBS structure (see inset in figure 3(b)) evidence the presence of a helix-like substructure. The TEM morphological analysis (figures 4(a)–(d)) in BSF-EuM: KerBS and KerST mixed suspensions still evidenced a colloidal background (bright scale) of dispersed particles where the two components cannot be clearly distinguished. However, the radial structure of KerST and of KerBS are greatly modified in the 1:4 case (a-e) and 4:1 (b-f) where the aggregation region exhibits similar features.

In both the 1:9 and 9:1 system the particle aggregation is modified by becoming more linearized, driven by the Keratin structure. Some peculiar arrangement of the 1:9 and 9:1 BSF-EuM:KerBS (figures 4(g) and (h)) have been observed with the internalization of the eumelanin in between the keratin filaments in the former and the external arrangements in the latter.

3.2. FT-IR results

In figure 5, the FT-IR taken on one component compares those already published on BSF-EuMel [57] and KerBS [63] with the data collected for the first time on KerST. This because the steam explosion method is not usually adopted for protein extraction and to verify that the process did not degrade the protein. On mixed component suspensions, the FT-IR of keratin spectrum always dominated the melanin one, notwithstanding the relative concentration ratios with no observable and relevant new spectral features. As a matter of example we add the comparison between FT-IR in mixed BSF-Eum: KerBS and BSF-EuM:KerST at a ratio of 1:4 (see figure in ESI) (see figure S1 in ESI).

The spectrum of BSF-EuM is characterized by several vibration bands, indicated in the figure 5 with the stars. A wide band in zone of 3200 cm^{-1} can be observed, corresponding to links vibration of the functional groups −OH and −NH2, 2918 cm^{-1} corresponding to the N–H stretching [83–87]. Specific eumelanin stretches were observed also between 1500–1400 cm^{-1}, which were attributed to the bending vibration of N–H and the stretching vibration of C–N (secondary amine) of an indolic [88]. The strong infrared band in the range of 1380–1240 cm^{-1} indicated the presence of a pyran ring [89]. Several eumelanin spectra have also included absorption bands between 1250–1180 cm^{-1}, caused by the stretching vibration of phenolic –OH groups [88]. The spectrum confirms that the extracted eumelanin is a eumelanin.

The spectra for KerST and KerBS exhibit the characteristics protein bands of Keratin. The absorption band at approximately 3300 cm^{-1}, is attributed to the stretching vibrations of N–H and O–H bonds and is associated with amide A [90]. Stretching vibrations of the C=O bonds, appearing between 1600 and 1700 cm^{-1}, are characteristic of the amide I band, which is linked to the secondary structure of keratin [91]. The bending vibration of N–H at 1520 cm^{-1} corresponds to amide II [92]. The stretching vibrations of C–N and C–H, along with the bending vibrations of N–H and C=O, occurring around 1220–1300 cm^{-1}, are related to amide III [93]. A notable difference between the two spectra is the sizeable reduction of the amide III signal components (1220–1300 cm^{-1}) and the vibrations present in the region between 700 and 1100 cm^{-1} visible in the KerBS sample. This range is highly sensitive to the presence of sulfur derivatives, suggesting that an increasing number of disulfide bonds have been reduced to form cysteic

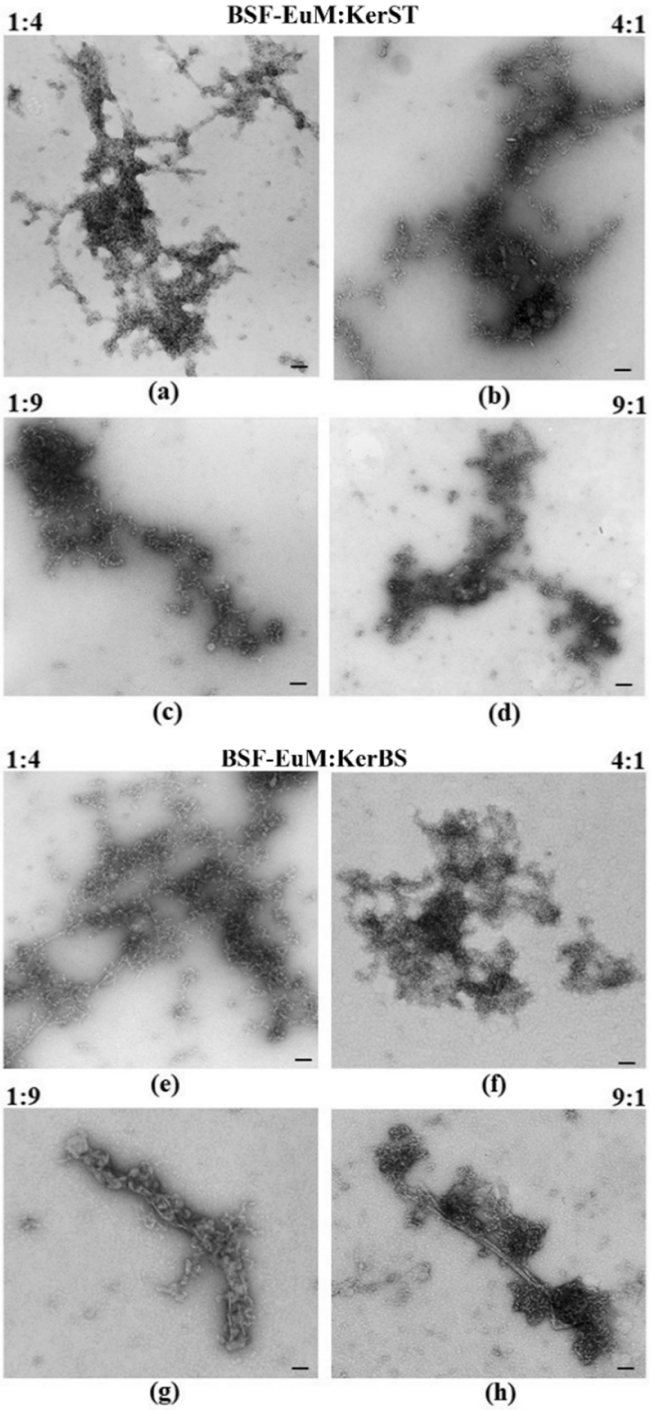

Figure 4. TEM micrographs of BSF-EuM:KerST (a)-(d) and BSF-EuM:KerBS (e)-(h) in different ratios. (Magnification 80.000 X, bar = 50nm). In figure 4(c) the different positioning of BSF-EuM around the KerBS ribbon is evidenced, showing the BSF-EuM internalization in KerBS in the former.

acid [91], which is related to the use of the metabisulfite method. From the above, the FT-IR analysis confirms that the underlying structure of keratin has been conserved and not destroyed by the extraction methods, though in the case of KerST less Sulphur groups are present.

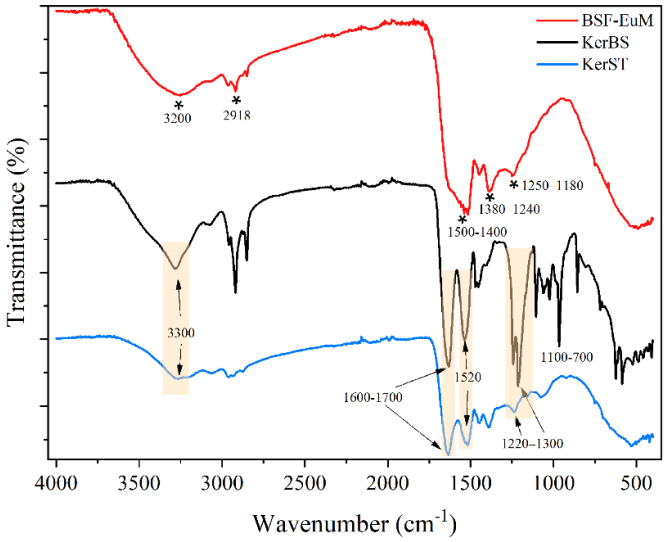

Figure 5. Comparison of FT-IR spectra for one component KerBS, KerST and BSF-EuM in powder form. The yellow boxes highlight the principal protein bands, while stars indicate the principal eumelanin vibration bands. The wavenumber corresponding to the vibration are also reported.

3.3. SAXS results

The profile collected for BSF-EuM (figure 6(a)) shows both an initial slope ($q < 0.1$ nm^{-1}) and a final slope ($1 < q < 3$ nm^{-1}) close to q^{-2}. suggesting them to fall within the case of an approximately planar geometry of both the overall dispersed aggregates and the individual particles [94]. In the intermediate q range (0.5–0.8 nm^{-1}) a knee is visible that corresponds to inhomogeneities in the dimension of particles with a radius of gyration of ∼2.5 nm, as assessed by an indirect Fourier transform in the range of 0.18–4 nm^{-1} to obtain a pair distance distribution function (p(r), inset of figure 6(a)). The model that provides an overall curve fit corresponds to a form factor of thin disks with diameter of 5.2 ± 0.1 nm and average thickness of 0.6 ± 0.3 nm, correlated by a mass fractal structure factor with fractal dimension of 2.9 and overall aggregate size above the limit imposed by the available angular range (>100 nm).

These dimensions for BSF-EuM are noteworthy. In previous x-ray diffraction literature from Cheng *et al* [95, 96], powdered eumelanin was also modeled to a similar disklike structure with lateral dimensions of 4–8 units of eumelanin, with 4 layers of stacking and a repeating dimension of ∼1.5 nm. In our results, it should be noted that the thickness of approximately 1 nm is poorly determined and with a high uncertainty due to the signal of the sample (being a 4 mg ml^{-1} diluted suspension in water rather than a powdered solid) reaching the water background level for $q > 5$ nm^{-1}. However, if a thickness equal or greater than 1.5 nm is imposed, the model visibly deviates from the data, and this suggests that the disks should be made by less than 5 layers of π-π/pancake bonded stacking structure [97].

In addition, our most probable modeled disk diameter (4 nm) is much wider than Cheng *et al*'s, suggesting that the BSF-EuM particles are extended 'floppy' sheets of material.

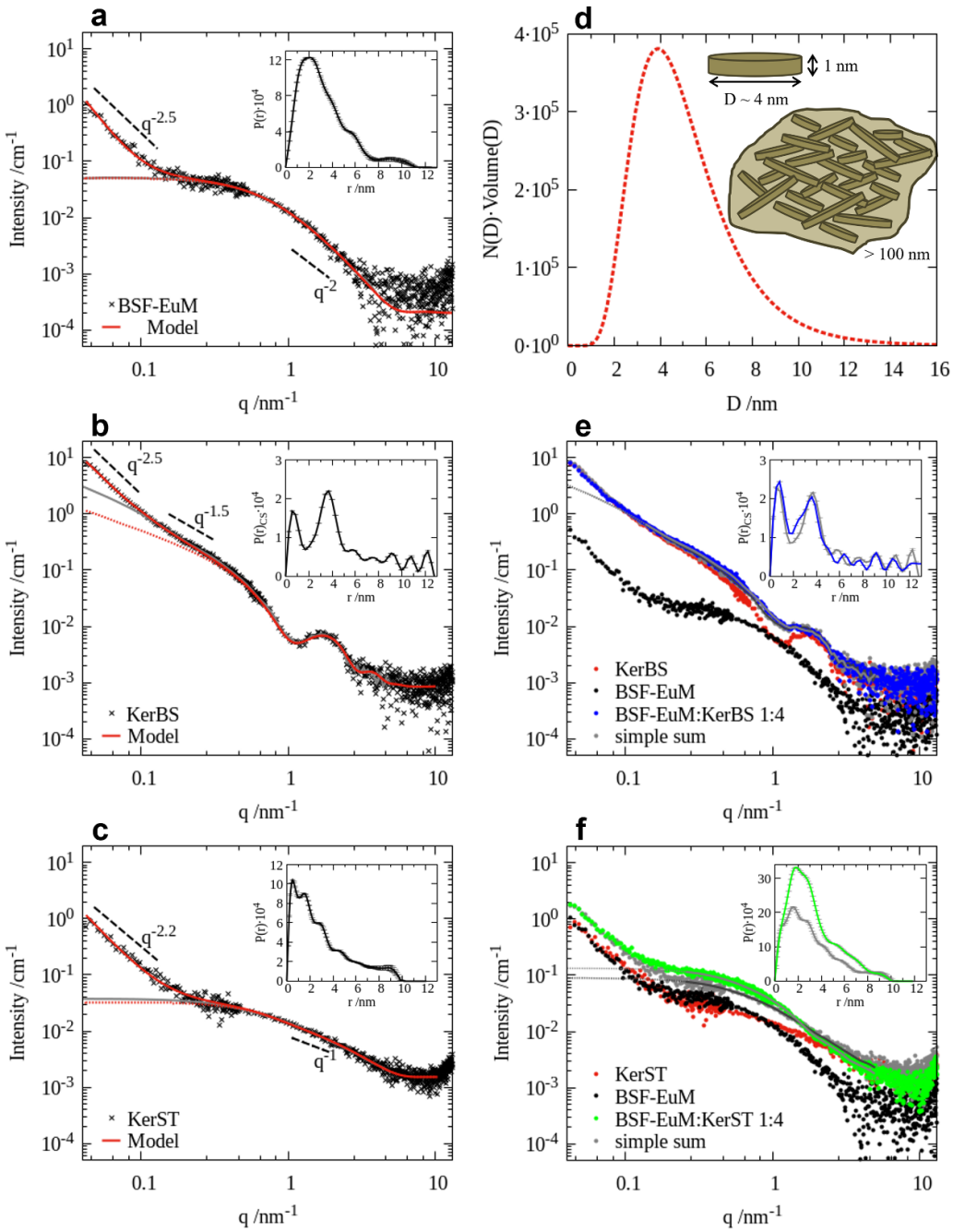

Figure 6. SAXS scattering curves of pure components (the black crosses represent raw data, the red line represent the calculated model curve, with the dotted portion only showing the form factor without structure factor): (a) BSF-EuM at 4 mg ml^{-1} concentration in water solution and (d) BSF-EuM size distribution of disk diameter that fits the data keeping fixed the disk thickness to 1 nm, is shown, together with a sketch of the model; (b) KerBS at 7.5 mg ml^{-1} concentration in water solution (c) KerST with a concentration of 17.5 mg ml^{-1} in water solution. (e) and (f) Superimposition on absolute units of the SAXS data of eumelanin (black dots), keratin (red dots) and their mixtures (blue or green dots), compared to simulated data obtained as a simple sum of the two components (grey dots): (e) eumelanin (BSF-EuM), sulphitolysis keratin (KerBS) and their mixture obtained in the BSF-EuM: KerBS 1:4 proportion; (f) eumelanin (BSF-EuM), steam explosion keratin (KerST) and their mixture obtained in the BSF-EuM: KerST 1:4 proportion. In all panels the insets show the pair distance distribution functions of the overall data ($P(r)$) or of the cross-section for elongated objects ($P_{CS}(r)$), and the corresponding fits to the data by indirect Fourier inversion are shown as solid grey lines in the main plots.

When inspecting Cheng *et al*'s data though, it should be noted that their data was obtained on dried eumelanin, both natural and synthetic, but at higher q ranges (10–100 nm^{-1}) where they also saw additional peaks, corresponding to much smaller characteristic distances, below 0.5 nm.

A better comparison to our data set would be the work of Gallas *et al* [98] and Littrell *et al* [99] where the authors did a SAXS study on various synthetic eumelanin, where similar concentrations and q ranges were employed. These works exhibit SAXS data with similar knee features as those reported here (figure 6(a)). What is interesting is that these authors determined stacked particles of thicknesses of ∼1 nm (3–4 layers), with disklike structures showing diameters of 5 nm. In this regard, the extent of the particles contained in the BSF-EuM sample correspond well with this synthetic eumelanin dispersed in water.

As a second pristine material to consider is the KerBS keratin from metabisulphite extraction [63]. In this case the best model for the data in figure 6(b), indicate a core-shell cylinder model, whose overall length extends above the limit imposed by the minimum scattering momentum detected (>100 nm). Additionally, there is a lower electron density of the core and higher electron density of the shell, compatibly with the higher sulphur content occurring on the keratin protofilament surface. The core radius assumes values from 1.2 nm to 3.3 nm according to a decaying size distribution that can accommodate a possible small number of bundled individual filaments within fibrils (<7), while the shell thickness is of the order of 0.8 nm. The deviation in the low q regime ($q < 0.15$ nm^{-1}) from the power law expected for rigid rods (close to $q^{-2.5}$ rather than q^{-1}) can be due to flexibility of individual fibrils or a degree of inter-fibril correlation. Such deviation can be reproduced by considering a mass fractal structure factor with dimensionality 2, characteristic object size of 13 nm and cut-off distance of 100 nm. Such a model is like what is observed in [94], which shows long ribbons with cross-sectional units of about 3 × 3 nm^2, hinting a possible preservation of the keratin protofilament structure by the extraction method.

Differently from KerBS, the scattering profile collected for KerST (figure 6(c)), does not show the features of a fibrillar structure, but has two characteristic slopes (close to q^{-1} for $q > 1.5$ nm and close to q^{-2} for q <0.2 nm^{-1}), and a knee in the intermediate range that would correspond to characteristic sizes of the order of 2 nm. A possible model used to represent the SAXS data is consisting of a form factor of a swollen coil, with radius of gyration of 1.8 nm and a self-avoiding behavior with Flory exponent close to 0.6 (rather than 0.5 for random walk), in conjunction with a fractal structure factor in which the individual object size is around 7.5 nm and the dimensionality is 2.5. Alternatively, the high q data is preferably interpreted in terms of compact particles rather than chain structures. The best fit was obtained with a spheroid model, which implies a pronouncedly prolate geometry (with axes 1.1 nm × 1.1 nm × 9 nm) rather than oblate and flat-like. In any case, the average size of individual scatterers is significantly smaller compared to the KerBS structure, probably due to the mechanical action of the extraction process and the fragmentation in elementary sections and unfolded peptide chains.

In these two latter cases of keratin a different power law was observed in the intermediate q range (around 0.1 nm^{-1}, approximately a length scale of 30 nm), corresponding to a transition from a preferentially 1D system (KerBS) to a 2–3D one (KerST).

For the mixed sample involving KerBS (BSF-EuM:KerBS (1:4), figure 6(e)) we find that the scattering profile of the mixture closely resembles the signal observed for KerBS, indicating that the fibrillar structure of the keratin is substantially preserved after interaction with eumelanin.

In this case, comparing the mixture data with simulated data as a simple sum of the two components, a small deviation can be appreciated in the q range 0.7–1.5 nm^{-1}. Observing the calculated pair distance distribution functions of the cross section, the deviation can be related to a change of the internal fibril electron density contrast (distances <5 nm), suggesting that the small eumelanin disks can be partially incorporated into the fibril structure. For the mixed sample involving KerST (BSF-EuM:KerST (1:4), figure 6(f)) no large structural transition of the eumelanin is detected, but the significantly higher scattering intensity of the mixture compared to a simple sum of the profiles of pure keratin and eumelanin samples suggests enhanced co-aggregation of the keratin extracted components within the eumelanin clusters, whose individual units preserve sizes of 5–6 nm.

3.4. Broadband dielectric spectroscopy

The BDS is recognized as a technique highly sensitive to dipolar interaction of water molecules (proton ions) on a wide set of materials [56, 77, 79] Among the others, its application has been widely used to provide deep insight on water-biopolymer and protein interaction, the former including BSF-Eumelanin as well [57]. In the first case, the examination was exclusively performed between water vapor molecule and BSF-EuM layer providing detailed information on the evolution of the dielectric response vs. hydration [57]. Water-protein interaction [56] has been also the subject of several studies adopting BDS. Since keratin belongs to the class of protein, BDS can be considered a suitable technique for studying its interaction with water. The structural information gained by TEM evidenced the formation of a homogenous colloidal suspension and regions where peculiar aggregation structures are observed. SAXS suggested enhanced co-aggregation of the keratin extracted components within the eumelanin clusters. The structural picture gathered via TEM and SAXS will take advantage of the BDS, suitable in providing more information on the effect of those structures via the dielectric relaxation and, much more, in a solvent dipolar system like water. In fact, the feasibility of spanning a wide range of frequency via BDS offers detailed insights into the AC response of a biopolymer mixture. In this framework, the BDS is intended to be the superposition of regions that respond to the frequency of the AC signal depending on their

extension and resulting in final relaxation observed in the spectra. As stated above, the slower relaxation depends on the linear extension of the aggregates the faster on the radial extension. (expr.10) Both regulate the dynamic of the ionic charges (counterions) leading to slow (condensed counterions) or fast (free counterion) ion charge dynamics. Therefore, these measurements are guided by dielectric polarization mechanisms, thus the 'geometrical' dimensions determined by using this approach may differ from those seen in SAXS and TEM.

The BDS results is particularly suitable in detecting the AC response of a biopolymer mixture in a solvent dipolar system like water. The ε' spectra, as seen on a linear *y*-axis scale (figure 7), show that each single component biomaterial suspension decreases their dielectric constant at a characteristic radial frequency, $\omega_{EP,}$ which signals the cut-off frequency of the electrode polarization (EP) effect [57, 100]. The EP attribution is justified by the criterion adopted consisting in the comparison between the real and imaginary part of the dielectric permittivity (ε', ε'') and conductivity (σ', σ'') (figure 8) where the corresponding peaks in the imaginary part of the dielectric constant (ε'') and conductivity (σ'') signals the full development of the EP [100] (figure 8).

Thus, these lower frequency ranges capture the behavior of the electrode and its influence on the material under investigation. These effects are electrode-material specific and is not intrinsic to the biopolymer per se, which make low frequency features less useful for interrogation [100, 101]. However, in our study we use the same set of electrodes and geometry, allowing us to make an accounting of the electrode effects and talk intelligibly about the material behavior in the sub-EP region. We note that the variation in ω_{EP} depends on the biopolymer and suggest a different extension (range) of the electrostatic forces acting on the ionic charge distribution, which regulates the screening length termed as Debye length [100, 102].

We also note that at high frequency the real component of the dielectric constant saturates to a value of ∼80 for all the suspensions, which is close to the background solvent of water [103].

It is noteworthy that qualitatively the unfiltered BSF-EuMUF and KerST and the filtered BSF-EuMF and KerBS are similar. Specifically, dispersion of KerST and unfiltered BSF-EuME reveals two visible relaxation peaks (figure 7(b)). The first one we attribute to a β-relaxation. Utilizing the elicited AC conductivity data alongside the permittivity leads us to attribute the second peak to the relaxation frequency of the electrode polarization (see figure 8) [100, 104]. In contrast, the spectra of filtered BSF-EuM and KerBS seems to exhibit only a single dominant relaxation process.

However, it is essential to recognize that the DC conductivity contribution to the relaxation processes is superimposed on the as received permittivity data, which may obscure the true dielectric dispersion and prevent complete resolution of relaxation processes [56].

Therefore, to gain accurate insights into the relaxation processes, we employ the $D_{\ln\omega}\varepsilon'(\omega) \approx \varepsilon''_{rel}$ representation to eliminate the DC contribution (figure 7(c)). Each spectrum exhibits unique features, although similarities emerge due to the same derivation of the dissolved/suspended components.

With the corrected data set, we employ a best fit approach adopting the HN formalism to $D_{\ln\omega}\varepsilon'(\omega) \approx \varepsilon''_{rel}$ with the fits shown in figure 9 and fitting parameters summarized in table S1. We clearly distinguish three HN distributions: HN_α, HN_β & HN_{EP} corresponding to three distinct relaxation processes, α, β & EP. These are now better resolved compared to their somewhat hindered representation in ε' or ε''. In the low-frequency region (0.1–10 Hz), the increase in $D_{\ln\omega}\varepsilon'(\omega) \approx \varepsilon''_{rel}$ evidence the tail of a slower α-relaxation with the frequency of the peak displaced close to the lower of the measurement range (see f_α values in table 2). This relaxation is representative of the slow motion in the solvent of larger aggregates and can be furthermore associated to the system viscosity [81, 106, 107]. The magnitude of the corresponding dielectric strengths increases in BSF-EuMF with respect to BSF-EuMUF, whereas in KerBS it is higher than in KerST.

The second component, which is in the medium-frequency range, is assigned as a β relaxation and is associated with the polymer local conduction via ionic charge hopping mechanisms [77, 80, 104]. In this specific case the hopping is water mediated and depends on the hydration [55]. Notably, β relaxation magnitudes and peak positions are the same in KerST and BSF-EuMUF, highlighting similar features in the hydration-mediated processes. This may be the result in both cases of the presence of residual impurities as recently evidenced by 13 C CP/Mas NMR spectra of BSF-MelEuM where an intense signal is present in the aliphatic region of BSF eumelanin [108, 109]. Inspecting the keratin data reveals that in KerBS the contribution of the β relaxation is smaller than either the EP or α relaxation. Additionally, the β relaxation has a broader frequency distribution. The lower relative effect of the β relaxation with respect to EP can be a consequence of the more hydrophobic nature of KerBS, which was observed to be less soluble in water. Again, this may be due to a higher presence of sulfur functionalization, leading to a more hydrophobic property.

Finally, the third component represents the EP, whose magnitude may be regarded as an index of the strength of the screening charge effect. Following what is declared in the TEM analysis, if we regard the suspensions as a colloidal one, these values estimate the extension of the ionic charge distribution from around the suspended particles to the medium, i.e. the Debye length L_D [102, 110]. In the present case, the calculation of L_D via expr. 6 returned values between 0.27 nm to 2.03 nm corresponding to free ionic charge concentrations of approximated 10^{20} cm^{-3} in BSF-EuMF to 10^{18} cm^{-3} in all the other systems (see table 2).

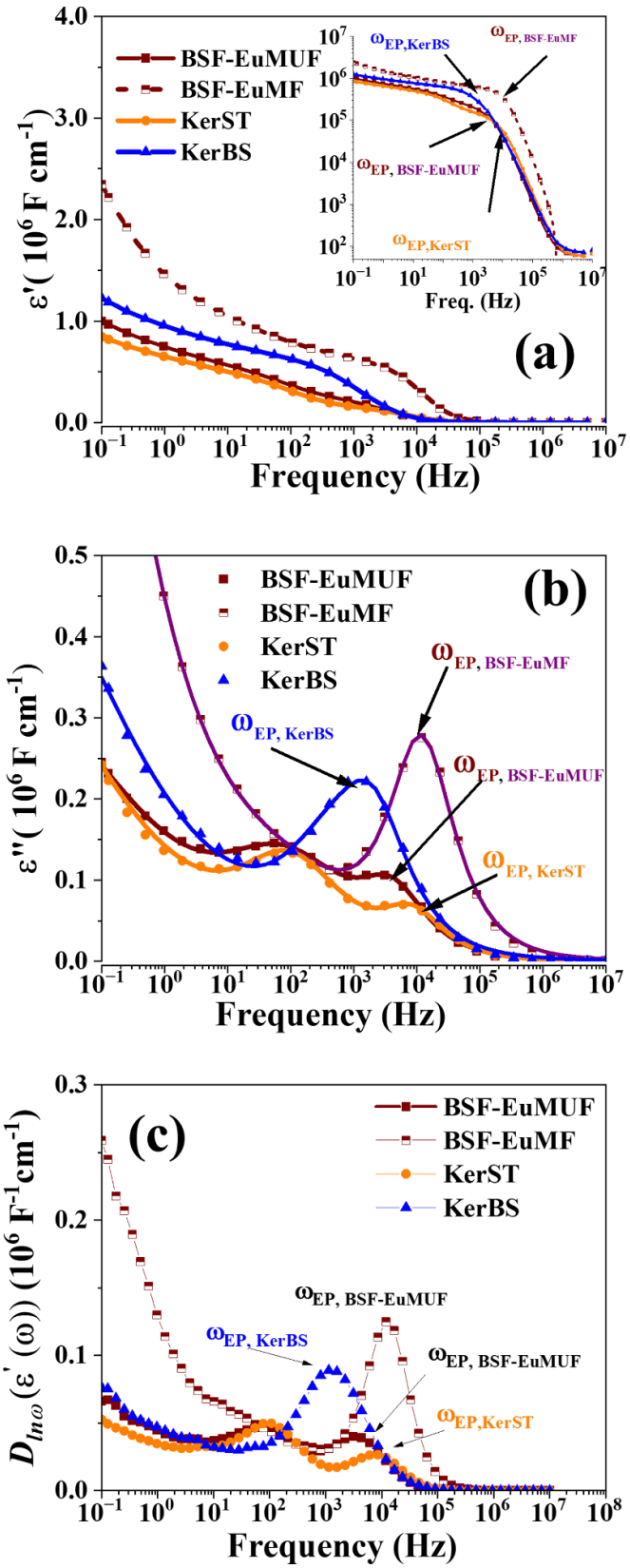

Figure 7. Linear scale representation of the dielectric permittivity dispersion relations of the single component suspension (conc. 10.0 mg ml^{-1}). Spectra include: (a) the real part of the dielectric permittivity ε' (inset shows log scale representation and radial frequency EP position; (b) the imaginary component ε''; $D_{\ln\omega}\varepsilon'(\omega) \approx \varepsilon''_{\text{rel}}(\omega)$. In the inset of (a) the log ε' vs. f show the radial frequency ω_{EP} corresponding to the drop of the ε' curve. We also indicate by $\omega_{EP,\text{ BSF-EuMUF}}$ and $\omega_{EP,\text{ BSF-EuMF}}$ the radial frequency position in unfiltered and filtered BSF-EuM suspensions. The radial frequency positions relate to that shown on the f-axis as $\omega = 2\pi f$.

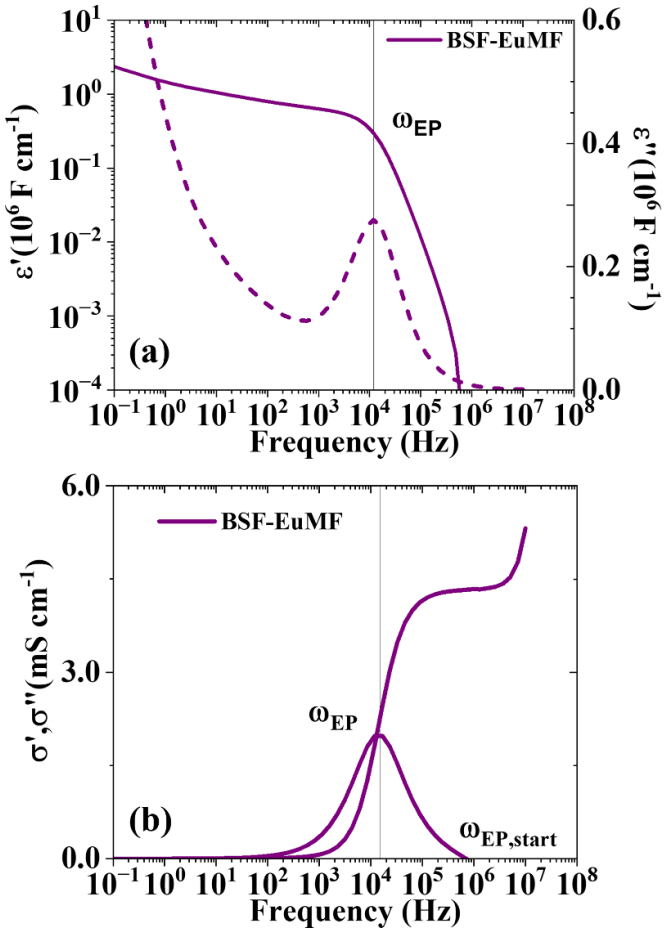

Figure 8. Representative example of the localization of the radial frequency $\omega_{EP} = 2\,\pi\,f_{EP}$ corresponding to the full development of the EP via the comparison between the real and imaginary part of the dielectric permittivity (8a, ε', ε'') and conductivity (8b, σ', σ''). The plateau in ε' is due to the charge accumulation at the electrodes and may mask possible other relaxations (see main text). The radial frequency of the frequency referred to the EP in ε'', and σ'' correspond to the drop in permittivity and to the onset in the σ' towards the plateau. In σ'' the radial frequency of the start of the EP has been indicated. The data refers to BSF-EuMF suspension (10 mg ml^{-1}) [104, 105].

The as calculated dielectric permittivity spectra for the two component suspensions are shown in figure S2, where substantial differences in the behaviors are manifested as compared to the single component spectra in figure 7.

More specifically, the changes revealed much relevant modification in the shape with respect to the single component, hinting furthermore a superposition of the contribution of relaxation of both components. Notably, the impact of the co-presence of the two polymers is evidenced by the shape modification becoming much more evident when increasing the eumelanin content. This is more noticeable in KerST mixed suspension (see 4:1 and 9:1, figure 10(c)) whereas in the case of KerBS mixed suspensions, this is noticeable in the 9:1 ratio (figure 11(d)). These behaviors agree with the SAXS results describing a higher co-aggregation in the case of KerST, that could be also the reasoning behind the behavior seen via BDS, furthermore evidencing the dependence vs. the increase of the melanin :keratin ratio.

To gain clarity, we again utilize the $D_{\ln\omega}\varepsilon'(\omega) \approx \varepsilon''_{rel}$ formalism to subtract the DC conductivity, with the corrected spectra shown in figures 10 and 11.

The significant alteration of the derivatives spectra $D_{\ln\omega}\varepsilon'(\omega) \approx \varepsilon''_{rel}$ can be related to the values calculated from the best fit dielectric parameters extracted vi the HN approach. These results (table 2) indicate that this is due to shifts in the peak frequencies, $f_{\alpha,\beta}$ (and correspondingly of the $\omega_{\alpha,\beta}$) of the α and β relaxations along with variations in the dielectric strength ($\Delta\varepsilon_{\alpha,\beta}$) parameters. These distributions are also influenced by changes in the a_i and b_i parameters (see values in table S1 and figure 12).

The behavior of the radial frequencies ω_α and ω_β of the relaxation peaks (symbols) vs. BSF-EuM:KerST(BS) ratio (figures 12(a) and (b)) suggests changes in the ion chain dynamics, ω_α, and local motion compared to those in the single component (straight lines) and more vs. the keratin ones. Specifically, a general increase is observed in ω_α (figure 12(a)) hinting the changes (i.e. reduced length) in the polymer chain dimension possibly due to the melanin introduction and/or a cooperative effect between both components. Conversely, the modification of the dynamics of the local motion, represented by the ω_β (figure 12(b)), is notable in the case of KerBS -based mixtures.

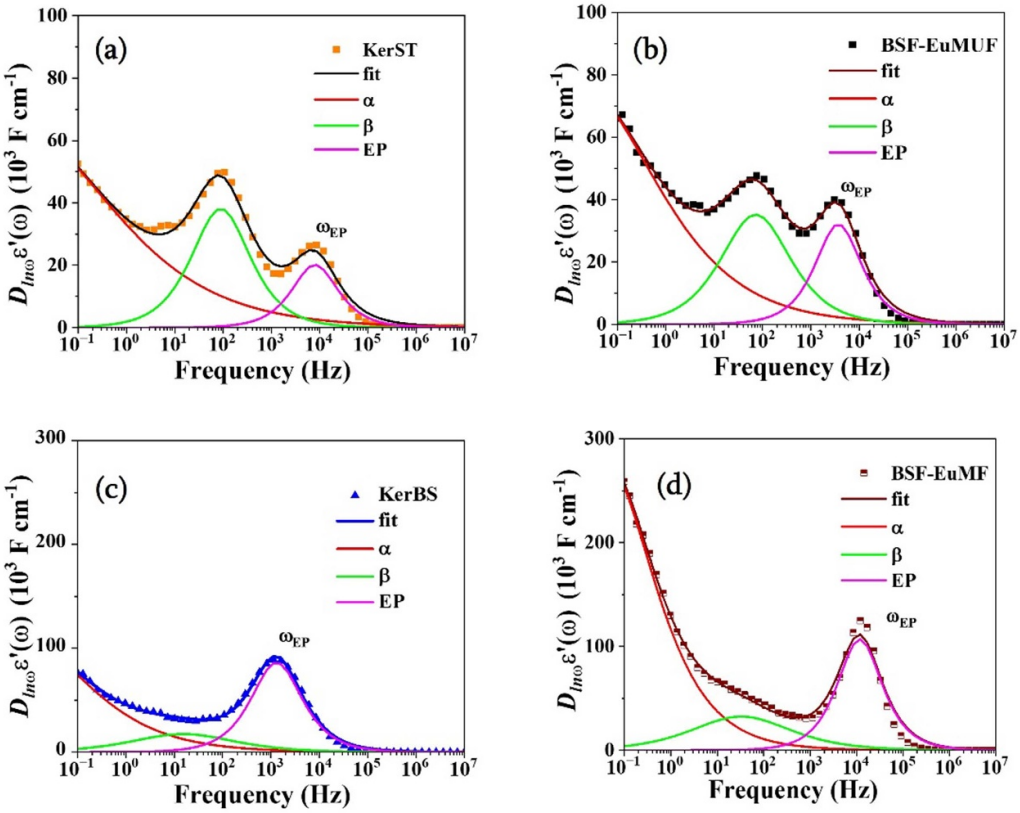

Figure 9. HN fits to the $D_{\ln\omega}\varepsilon'(\omega)$ representation of the single material/solvent suspensions (10.0 mg ml^{-1}). (a) KerST spectra; (b) KerBS spectra; (c) BSF-EuMUF spectra; (d) BSF-EuMF spectra. The three relaxations are represented in distinct colors: red for α-relaxation, green for β relaxation and magenta for EP relaxation. The corresponding HN parameters are listed in table S1).

The ω_{EP} in mixed suspensions display values generally lowering vs the BSF-EuM:KerST(BS) ratio (figure 12(c)). This effect together with the lowering of the $\Delta\varepsilon_{EP}$ implies a lower strength of the electrode polarization effect and lower ionic charge density (n in table 2) manifesting itself by the increase in the Debye length L_D particularly evident with respect to BSF-EuMF dipolar relaxation [106].

Inspecting the peak frequency positions and calculating l_α and l_β through the diffusivities of the 'condensed' $D_{ion,\alpha}$ and free counterion density $D_{ion,\beta}$ provided further insight on the interaction in one and mixed component with water. In single component suspensions, the two keratin systems show similar ω_α (f_α) values whereas variation have been observed in ω_β (f_β). These returned similar dimensions of the particle aggregates l_α, and different radial dimension i.e. ion charge hopping distance, l_β (table 2) [80, 81].

The former can be explained as due to the similar extension/length of the keratin rod-like aggregates and polymer chain motion features; the latter being related to ionic charge local motion can be due to the more hydrophobic properties of KerBS in water due to the local presence of a higher Sulphur functionalized surface with respect to KerST as also evidenced by FTIR results.

The lower values of l_α and the corresponding values of $D_{ion,\alpha}$ in almost all mixed suspensions vs. keratin suggest that the dielectric response modifies in water due to reciprocal effect of eumelanin on the structure of the keratin aggregate. Furthermore, this let to hypothesize the increase of the 'condensed' proton counterion density binding with the ionic dipoles on keratin backbone, thus explaining the blue shift of the radial frequencies ω_α [111]. Also, l_α being related to the α-relaxation, this let to argue that the variation may affect suspension viscosity [106, 112].

Moreover, we observe the increase l_β i.e. hopping distance, vs. the increase of the relative eumelanin content with respect to keratin, meaning that the hopping is slowed down.

The analysis of the dielectric strengths values shows an overall strong reduction of the $\Delta\varepsilon_\alpha$ (from 10^6 to 10^5 F cm^{-1}) and $\Delta\varepsilon_{EP}$ (from 10^5 to 10^4 F cm^{-1} with respect to the single component one (see table S1), whereas the magnitude of $\Delta\varepsilon_\beta$ is much less affected. The lower values of $\Delta\varepsilon_\alpha$, further underlining the reciprocal effect of the two biopolymers in affecting the cooperative motion and the dipolar relaxation of each single component [106].

Finally, although the measured AC conductivities fall in the range 10^{-5} S cm^{-1}÷10^{-3} S cm^{-1} in all suspensions, either in one component and mixed ones, (figure 13) a lowering of the values of the DC values (value at the plateau in the real component σ') has been found in mixed suspension especially with respect to BSF-EuMF. This suggest that keratin insertion is the main component limiting, via proton counterion condensation the free ionic charge transport. The lowering of the DC conductivity, combined with the changes in l_α, hints possible keratin-vehiculated plasticizing effect [113].

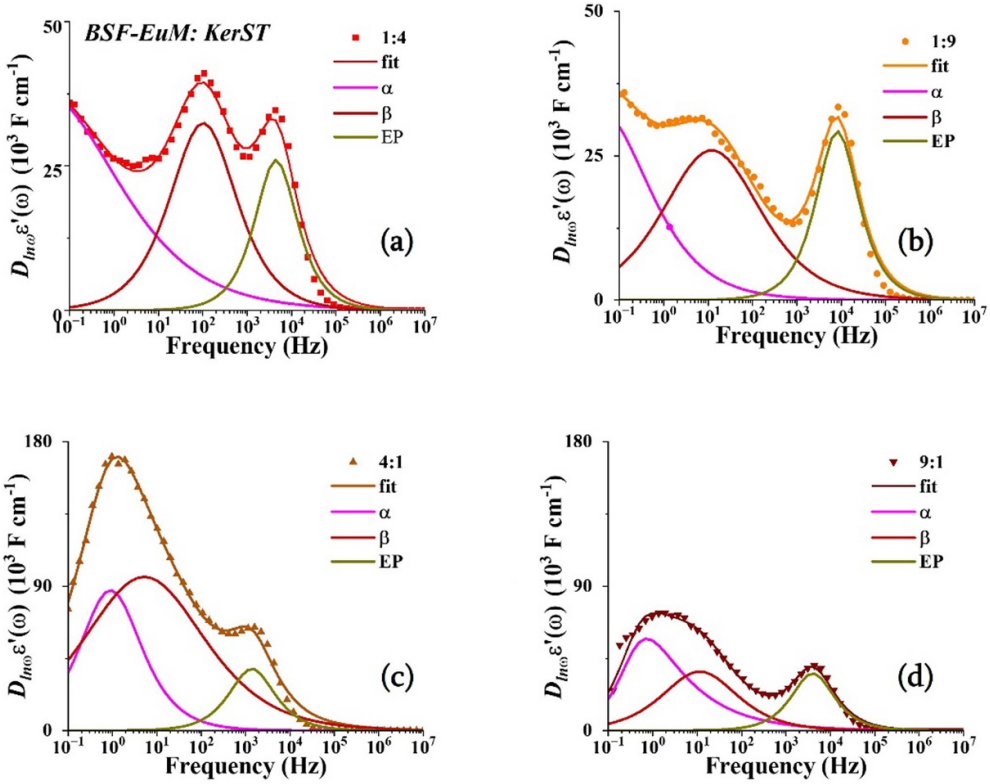

Figure 10. The $D_{\ln\omega}\varepsilon'(\omega)$ spectra with associated HN fits for the two component suspensions of BSF-EuM and KerST for different ratios: (a) 1:4, (b) 1:9, (c) 4:1, (d) 9:1. The three relaxations peaks are represented by distinct colors: magenta—α-relaxation, wine—β relaxation, dark yellow—EP relaxation. The corresponding HN parameters are reported in table S1.

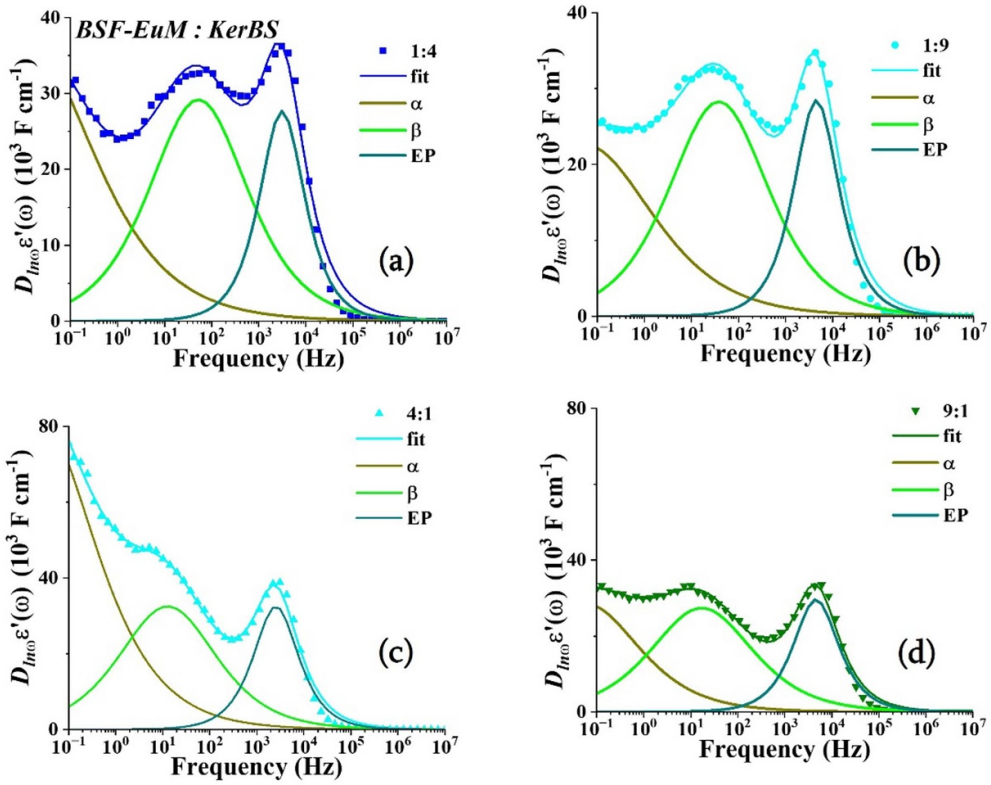

Figure 11. The $D_{\ln\omega}\varepsilon'(\omega)$ spectra with associated HN fits for the two component suspensions of BSF-EuM and KerBS for different ratios; (a) 1:4, (b) 1:9, (c) 4:1, (d) 9:1. The three relaxations peaks are represented by distinct colors: dark yellow—α-relaxation, green—β relaxation, dark cyan—EP relaxation. The corresponding HN parameters are reported in table S1

Table 2. Free ionic charge concentrations, n, and Debye lengths, L_D, of one the component and mixed suspensions calculated via expr. 5 and 6; values of diffusivity of condensed $D_{ion\alpha}$ and free $D_{ion\beta}$ counterion diffusivity together with the estimated rod length l_α and hopping/radial distance l_β.* BSF-EuM:KerST mass ratio.

Suspensions	n (10^{18}cm^{-3})	L_D (nm)	ω_{EP} (rad s^{-1})	ω_α (rad s^{-1})	ω_β (rad s^{-1})	$D_{ion\alpha}$ (10^{-10} cm^{2}s^{-1})	$D_{ion\beta}$ (10^{-8} cm^{2}s^{-1})	Ratio*	l_α (μm)	l_β (μm)
BSF-EuMUF	1.27	1.92	23 364	0.09	457	1.67	7.6	—	2.60	0.79
BSF-EuMF	164	0.27	73 529	0.21	205	0.05	0.03	—	0.30	0.08
KerST	0.96	2.12	52 910	0.01	633	2.19	13	—	9.00	0.88
KerBS	1.51	2.03	14 285	0.01	2994	2.09	46	.	8.00	0.76
BSF-EuM:KerST										
	1.04	2.35	51546	0.23	76	0.96	0.84	0.11	1.26	0.64
S16 1:9	1.00	2.63	27 778	0.15	667	1.20	10.9	0.25	1.75	0.78
S15 1:4	2.46	2.31	8696	5.62	33	3.13	0.91	4.00	0.45	1.04
S17 4:1	1.13	2.66	25 189	3.05	48	19.0	1.35	9.00	1.58	1.03
S18 9:1					—					
BSF-EuM:KerBS										
	1.23	2.57	28571	0.33	240	0.80	2.20	0.11	0.95	0.58
S22 1:9	1.01	2.98	19 724	0.06	680	0.82	9.70	0.25	2.30	0.73
S21 1:4	1.03	2.49	16 077	0.12	80	2.26	1.20	4.00	2.60	0.77
S23 4:1	1.60	1.64	28 902	0.37	107	0.98	2.30	9.00	1.00	0.90
S24 9:1										

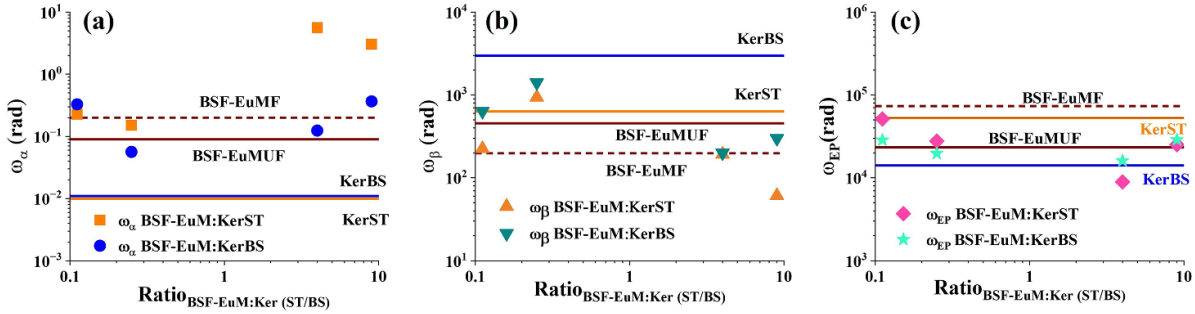

Figure 12. Comparison between the relaxation frequencies determined by expr. 9a in single component (straight line) and mixed suspensions (symbols).

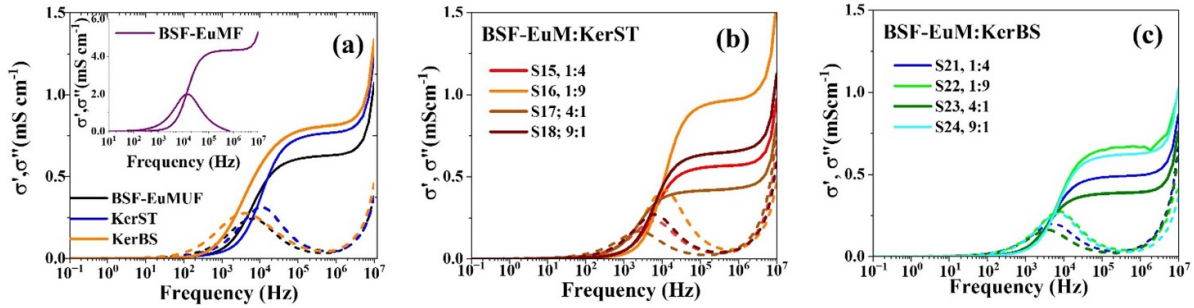

Figure 13. Real (σ') and imaginary (σ'') parts of the AC conductivity of one component (a) and mixed suspension of BSF:EuMF :KerST (b) and BSF:EuMF :KerBS (c). The inset of (a) shows the AC conductivity of BSF:EuM. The mixed suspensions are labeled following table 1.

4. Conclusions

The chemical, structural and dielectric properties of powders and water-based suspensions of eumelanin and two types of keratins derived from organic waste via sustainable processes are discussed. The examined suspensions included both single component and their mix at selected BSF-Mel: Ker mass ratios. FTIR on biopolymer powders together with SAXS, TEM and BDS on suspensions provided comprehensive insight of their properties and correlation between chemistry, structure and dielectric properties.

As a whole, the study discussed the fundamental properties of water-based suspensions made up of one and mixed Eumelanin-Keratin biopolymer and extends the one(s) on BSF-EuM [57] and related devices all derived in the framework of the CE approach [19].

The adopted techniques enabled to evidence specific features of the suspensions under different observation points. In one component suspensions

- SAXS modeling returned BSF-EuM aggregation confirm the π-π/pancake structure [97]. In KerST and KerBS the derived geometrical extension returned a 2-dimensional structure in KerST opposed to a more linear structure of KerBS.
- TEM results were in line with SAXS i.e. aggregation of nanoparticles in BSF-EuM, a planar star-like structure in KerST and a linear one in KerBS
- BDS responses differ in each biopolymer, with some similarities between unfiltered and filtered BSF-EuM with KerST and KerBS, due to residual proteins. The values of l_α and l_β confirms TEM and SAXS results.

In the two-component suspensions:

- the SAXS modeling evidenced a superposition of independent contributes, with higher coaggregation in the case of KerST
- TEM confirms the superposition seen via SAXS modeling with BSF-EuM eumelanin surrounding KerST loosing the star light features; in BSF-EuM:KerBS mixtures 1:9 and 9:1 eumelanin internalization (1:9) or surrounding the KerBS bent (9:1) are found.
- TEM in line with SAXS suggests biopolymers aggregate in a different geometry when are both in water, thus explaining the carrier hopping lengths l_α and radial distances l_β extracted from BDS data.
- BDS spectra evidence a cooperative effects via a substantial different behavior respect to the one component, that is more expressed when increasing the eumelanin content (i.e. BSF-EuM:KerST (4:1) and (9:1)).
- The DC conductivities hint a keratin vehiculated plasticizing effect.

Finally, the production of disposable or medium-long time working devices by adopting deposition techniques from such aqueous liquid phase suspensions is already in progress, with promising results that will be the subject of our future research papers

Data availability statement

All data that support the findings of this study are included within the article (and any supplementary files).

Acknowledgments

M A and P F A acknowledge the Italian Ministry of University and Research (MUR) PONa3_00369 SISTEMA.

D A thanks Italian National Recovery and Resilience Plan (NRRP), funded by the European Union—NextGenerationEU (Mission 4, Component 2, Investment 3.1—Area ESFRI Energy—Call for tender No. 3264 of 28-12-2021 of Italian University and Research Ministry (MUR), Project ID IR0000007 'NEFERTARI—', MUR Concession Decree No. 243 del 04/08/2022, CUP B53C22003070006,). Views and opinions expressed are however those of the author(s) only and do not necessarily reflect those of the European Union or the European Commission. Neither the European Union nor the European Commission can be held responsible for them.

A B M aknowledges the support by the UKRI Research Partnerships Investment Fund through the Centre for Integrative Semiconductor Materials'.

Author contributions

Conceptualization, M A, S M, A B M and R G;

Methodology, M A, S M, J W P, R G, A D G, D A A D S, A G, S M,F L,C L

Software, M A, S M,A D S, P F:A;

Validation M A, A B M, R G;

Formal analysis, A B M, M A,A D G;

Investigation, M A, S M,

Resources, M A, J W P, G L, F L,C L, P F A, A D S, R,G;

Data curation: M A.,A B M, A D G,S M;

Writing—**O**riginal draft preparation: M A; A B M;

Writing—**R**eview and **E**diting, M A,A B M;

Visualization, M A, P F A, S M; supervision, M A, A B M; **P**

Project administration, M A, P F A, A B M, R G;

Funding acquisition, M A, P F A, A B M, R G

All authors have read and agreed to the published version of the manuscript.

Fundings

For R G and S M: this work is funded by European Union—NextGenerationEU under the Italian Ministry of University and Research (MUR) National Innovation Ecosystem grant ECS00000041—VITALITY—Spoke 9.

For A B M: this work was also supported by the UKRI Research Partnerships Investment Fund through the Centre for Integrative Semiconductor Materials.'

For P.F.A and D.A.: this work was supported by Regione Puglia, Riparti—POC PUGLIA FESRT-FSE 2014/2020.

Conflict of interest

'The authors declare no conflicts of interest'.

ORCID iDs

Marianna Ambrico https://orcid.org/0000-0002-0568-6860
Sara Mattiello https://orcid.org/0009-0000-9601-4703
Albertus Bernardus Mostert https://orcid.org/0000-0002-9590-2124
Jun Wei Phua https://orcid.org/0009-0002-1763-0861
Domenico Aceto https://orcid.org/0000-0002-5748-8962
Paolo F Ambrico https://orcid.org/0000-0002-2455-6949
Alessandro Guzzini https://orcid.org/0009-0006-2166-7391
Angelo De Stradis https://orcid.org/0000-0003-1624-2365
Federico Liuzzi https://orcid.org/0000-0001-9890-8014
Carlo Santulli https://orcid.org/0000-0002-1686-4271
Giulio Lupidi https://orcid.org/0000-0001-9452-0741
Alessandra Del Giudice https://orcid.org/0000-0002-1916-8300
Roberto Gunnella https://orcid.org/0000-0003-4739-6375

References

[1] United Nations Development Programm-Climate Promise 2023 What is Circular Economy and why does it matter? (available at: https://climatepromise.undp.org/news-and-stories/what-is-circular-economy-and-how-it-helps-fight-climate-change)

[2] Jane G *et al* (European Compost Network ECN e.V.) 2022 Compost and digestate for a circular bioeconomy *ECN Data Report 2022 Compost and Digestate for a Circular Bioeconomy*

[3] Baldé C P, Forti V, Gray V, Kuehr R and Stegmann P 2017 *The Global E-waste Monitor 2017: Quantities, Flows, and Resources* (United Nations University (UNU), International Telecommunication Union (ITU) & International Solid Waste Association (ISWA))

[4] Garam B *et al* (WEF (World Economic Forum) and PACE (Platfor for accelerating Circular Economi)) 2019 *A New Circular Vision for Electronics Time for a Global Reboot* United Nation E-Waste Coalition

[5] Mozhiarasi V and Natarajan T S 2022 Slaughterhouse and poultry wastes: management practices, feedstocks for renewable energy production, and recovery of value added products *Biomass Convers. Biorefin* **12** 1–24

[6] Malviya R and Sundram S 2023 *Engineering Materials Engineered Biomaterials Synthesis and Applications* ed R Malviya and S Sundram (Springer)

[7] Paulin J V, Albano L G S, Camargo D H S, Pereira M P, Bregadiolli B A, Graeff C F O and Bufon C C B 2022 Eumelanin-based multisensory platform: a case of study for photolithographic patterning *Appl. Mater. Today* **28** 101525

[8] Migliaccio L, Aprano S, Iannuzzi L, Maglione M G, Tassini P, Minarini C, Manini P and Pezzella A 2017 Eumelanin–PEDOT:PSS complementing En Route to mammalian-pigment-based electrodes: design and fabrication of an ITO-Free organic light-emitting device *Adv. Electron. Mater.* **3** 1600342

[9] D'Amora U *et al* 2022 Eumelanin from the black soldier fly as sustainable biomaterial: characterisation and functional benefits in tissue-engineered composite scaffolds *Biomedicines* **10** 2945
[10] Placone J K, Navarro J, Laslo G W, Lerman M J, Gabard A R, Herendeen G J, Falco E E, Tomblyn S, Burnett L and Fisher J P 2017 Development and characterization of a 3D printed, keratin-based hydrogel *Ann. Biomed. Eng.* **45** 237–48
[11] Patil A B *et al* 2020 Tailoring the meso-structure of gold nanoparticles in keratin-based activated carbon toward high-performance flexible sensor *Nanomicro Lett.* **12** 1–11
[12] Shen B, Zhang D, Wei Y, Zhao Z, Ma X, Zhao X, Wang S and Yang W 2019 Preparation of Ag doped keratin/PA6 nanofiber membrane with enhanced air filtration and antimicrobial properties *Polymers* **11** 1–13
[13] Lazarus B S, Chadha C, Velasco-Hogan A, Barbosa J D V, Jasiuk I and Meyers M A 2021 Engineering with keratin: a functional material and a source of bioinspiration *iScience* **24** 102798
[14] Feroz S, Muhammad N, Ranayake J and Dias G 2020 Keratin—Based materials for biomedical applications *Bioact. Mater.* **5** 496–509
[15] Hamouche H, Makhlouf S, Chaouchi A and Laghrouche M 2018 Humidity sensor based on keratin bio polymer film *Sens. Actuators* A **282** 132–41
[16] Nowogrodski C, Simon I, Magdassi S and Shoseyov O 2020 Fabrication of second skin from keratin and melanin *Polymers* **12** 1–13
[17] Lin Q, Hao S, Hu W, Wang M, Zang Z, Zhu L, Du J and Tang X 2019 Human hair keratin for physically transient resistive switching memory devices *J. Mater. Chem.* C **7** 3315–21
[18] Pan J, Xia Z, Deng N, Chen L, Zhang H, Lu Y, Liu Y and Gao H 2023 Eumelanin-inspired nanomaterials in electrochemical energy storage devices: a review *Chem. Eng. J.* **452** 138607
[19] Krebsbach P, Rincón-Iglesias M, Pietsch M, Henel C, Lanceros-Mendez S, Phua J W, Ambrico M and Hernandez-Sosa G 2024 Inkjet-printed bio-based melanin composite humidity sensor for sustainable electronics *ACS Appl. Mater. Interfaces* **16** 42555–65
[20] Ischia M, Wakamatsu K, Briganti S, Kovacs D, Meredith P, Pezzella A, Sarna T, Simon J D and Ito S 2013 Melanins and melanogenesis: methods, standards, protocols *Pigment Cell Melanoma Res.* **26** 616–33
[21] Zucca F A *et al* 2004 The neuromelanin of human substantia nigra: physiological and pathogenic aspects *Pigment Cell Res.* **17** 610–7
[22] Bush W D, Garguilo J, Zucca F A, Albertini A, Zecca L, Edwards G S, Nemanich R J and Simon J D 2006 The surface oxidation potential of human neuromelanin reveals a spherical architecture with a pheomelanin core and a eumelanin surface *Proc. Natl Acad. Sci.* **103** 14785–9
[23] Meredith P, Powell B J, Riesz J, Nighswander-Rempel S P, Pederson M R and Moore E G 2006 Towards structure-property-function relationships for eumelanin *Soft Matter* **2** 37–44
[24] Solano F 2014 Melanins: skin pigments and much more—types, structural models, biological functions, and formation routes *New J. Sci.* **2014** 1–28
[25] Paulin J V, Coleone A P, Batagin-Neto A, Burwell G, Meredith P, Graeff C F O and Mostert A B 2021 Melanin thin-films: a perspective on optical and electrical properties *J. Mater. Chem.* C **9** 8345–58
[26] Felix C C, Hyde J S, Sarna T and Sealy R C 1978 Interactions of melanin with metal ions. Electron spin resonance evidence for chelate complexes of metal ions with free radicals *J. Am. Chem. Soc.* **100** 3922–6
[27] Al Khatib M, Costa J, Baratto M C, Basosi R and Pogni R 2020 Paramagnetism and relaxation dynamics in melanin biomaterials *J. Phys. Chem.* B **124** 2110–5
[28] Vasileiou T and Summerer L 2021 Vasileiou T and Summerer Erratum: a biomimetic approach to shielding from ionizing radiation: the case of melanized fungi *PLoS One* **16** e0257068
[29] Vasileiou T and Summerer L 2020 A biomimetic approach to shielding from ionizing radiation: the case of melanized fungi *PLoS One* **15** e0229921
[30] Mostert A B 2022 The importance of water content on the conductivity of biomaterials and bioelectronic devices *J. Mater. Chem.* B **10** 7108–21
[31] Sheliakina M, Mostert A B and Meredith P 2018 An all-solid-state biocompatible ion-to-electron transducer for bioelectronics *Mater. Horiz.* **5** 256–63
[32] Abramov P A, Zhukov S S, Savinov M, Mostert A B and Motovilov K A 2023 The influence of copper ions on the transport and relaxation properties of hydrated eumelanin *Phys. Chem. Chem. Phys.* **25** 11601–12
[33] Mostert A B, Rienecker S B, Sheliakina M, Zierep P, Hanson G R, Harmer J R, Schenk G and Meredith P 2020 Engineering proton conductivity in melanin using metal doping *J. Mater. Chem.* B **8** 8050–60
[34] Nozella N L, Lima J V M, de Oliveira R F and de Oliveira Graeff C F 2023 Melanin/PEDOT:PSS blend as organic mixed ionic electronic conductor (OMIEC) for sustainable electronics *Mater. Adv.* **4** 4732–43
[35] Xu R, Gouda A, Caso M F, Soavi F and Santato C 2019 Melanin: a greener route to enhance energy storage under solar light *ACS Omega* **4** 12244–51
[36] Kumar P, Di Mauro E, Zhang S, Pezzella A, Soavi F, Santato C and Cicoira F 2016 Melanin-based flexible supercapacitors *J. Mater. Chem.* C **4** 9516–25
[37] Kim Y J, Wu W, Chun S E, Whitacre J F and Bettinger C J 2013 Biologically derived melanin electrodes in aqueous sodium-ion energy storage devices *Proc. Natl Acad. Sci. USA* **110** 20912–7
[38] Paulin J V, Fernandes S L and Graeff C F O 2021 Solid-state electrochemical energy storage based on soluble melanin *Electrochem* **2** 264–73
[39] Ambrico M, Ambrico P F, Ligonzo T, Cardone A, Cicco S R, Lavizzera A, Augelli V and Farinola G M 2012 Memory-like behavior as a feature of electrical signal transmission in melanin-like bio-polymers *Appl. Phys. Lett.* **100** 253702
[40] Ambrico M, Cardone A, Ligonzo T, Augelli V, Ambrico P F, Cicco S, Farinola G M, Filannino M, Perna G and Capozzi V 2010 Hysteresis-type current–voltage characteristics in Au/eumelanin/ITO/glass structure: towards melanin based memory devices *Org. Electron.* **11** 1809–14
[41] Wahab A, Gogurla N, Park J Y and Kim S 2022 Architecting silk protein and melanin for photoresponsive and self-healable optoelectronic skins *Adv. Mater. Technol.* **7** 2101271
[42] Nam H J, Cha J, Lee S H, Yoo W J and Jung D Y 2014 A new mussel-inspired polydopamine phototransistor with high photosensitivity: signal amplification and light-controlled switching properties *Chem. Commun.* **50** 1458–61
[43] Xiao M, Li Y, Zhao J, Wang Z, Gao M, Gianneschi N C, Dhinojwala A and Shawkey M D 2016 Stimuli-responsive structurally colored films from bioinspired synthetic melanin nanoparticles *Chem. Mater.* **28** 5516–21
[44] Wu T F, Wee B H and Hong J D 2015 An ultrasensitive and fast moisture sensor based on self-assembled

dopamine-melanin thin films *Adv. Mater. Interfaces* **2** 1500203
[45] Silva M P D, Fernandes J C, De Figueiredo N B, Congiu M, Mulato M and Graeff C F D O 2014 Melanin as an active layer in biosensors *AIP Adv.* **4** 127149
[46] Tehrani Z, Whelan S P, Mostert A B, Paulin J V, Ali M M, Ahmadi E D, Graeff C F O, Guy O J and Gethin D T 2020 Printable and flexible graphene pH sensors utilising thin film melanin for physiological applications *2D Mater.* **7** 024008
[47] Whelan S P, Tehrani Z, Peacock M, Paulin J V, Guy O and Gethin D 2022 Investigation into the suitability of screen printed graphene-melanin pH sensors for use in bacterial culturing applications *J. Electroanal. Chem.* **904** 115868
[48] Di Mauro E, Rho D and Santato C 2021 Biodegradation of bio-sourced and synthetic organic electronic materials towards green organic electronics *Nat. Commun.* **12** 1–10
[49] Wang B, Yang W, McKittrick J and Meyers M A 2016 Keratin: structure, mechanical properties, occurrence in biological organisms, and efforts at bioinspiration *Prog. Mater. Sci.* **76** 229–318
[50] Shavandi A, Silva T H, Bekhit A A and Bekhit A E D A 2017 Keratin: dissolution, extraction and biomedical application *Biomater. Sci.* **5** 1699–735
[51] Hong L and Simon J D 2007 Current understanding of the binding sites, capacity, affinity, and biological significance of metals in melanin *J. Phys. Chem.* B **111** 7938–47
[52] Bento-Lopes L, Cabaço L C, Charneca J, Neto M V, Seabra M C and Barral D C 2023 Melanin's journey from melanocytes to keratinocytes: uncovering the molecular mechanisms of melanin transfer and processing *Int. J. Mol. Sci.* **24** 11289
[53] Amdursky N, Głowacki E D and Meredith P 2019 Macroscale biomolecular electronics and ionics *Adv. Mater.* **31** 1802221
[54] Shim J S, Rogers J A and Kang S K 2021 Physically transient electronic materials and devices *Mater. Sci. Eng.* R **145** 100624
[55] Schwan H P 1957 Electrical properties of tissue and cell suspensions *Adv. Biol. Med. Phys.* **5** 147–209
[56] Nakanishi M and Sokolov A P 2015 Protein dynamics in a broad frequency range: dielectric spectroscopy studies *J. Non– Cryst. Solids* **407** 478–85
[57] Ambrico M, Mostert A B, Ambrico P F, Phua J, Mattiello S and Gunnella R 2024 Exploring ion mobility mechanisms in poly indolequinone polymers: a case study on black soldier fly melanin *J. Phys. D: Appl. Phys.* **57** 265303
[58] Phua J W and Ottenheim C J H 2021 A method for obtaining melanin from invertebrate biomass and the product obtained therefrom US20230127563A1
[59] Shen Q, Ma Y, Qin X, Guo Y and Zhang C 2024 Steam explosion as a green method to treat animal waste: a mini-review *Process. Saf. Environ. Prot.* **181** 43–52
[60] Caporusso A, De Bari I, Liuzzi F, Albergo R, Valerio V, Viola E, Pietrafesa R, Siesto G and Capece A 2023 Optimized conversion of wheat straw into single cell oils by Yarrowia lipolytica and Lipomyces tetrasporus and synthesis of advanced biofuels *Renew. Energy* **202** 184–95
[61] Tonin C, Zoccola M, Aluigi A, Varesano A, Montarsolo A, Vineis C and Zimbardi F 2006 Study on the conversion of wool keratin by steam explosion *Biomacromolecules* **7** 3499–504
[62] Kawasaki H, Shimanouchi T and Kimura Y 2019 Recent development of optimization of lyophilization process *J. Chem.* **2019** 1–14
[63] Mattiello S, Guzzini A, Del Giudice A, Santulli C, Antonini M, Lupidi G and Gunnella R 2023 Physico-chemical characterization of keratin from wool and chicken feathers extracted using refined chemical methods *Polymers* **15** 181
[64] Wang K, Li R, Ma J H, Jian Y K and Che J N 2016 Extracting keratin from wool by using l-cysteine *Green Chem.* **18** 476–81
[65] Sinkiewicz I, Śliwińska A, Staroszczyk H and Kołodziejska I 2017 Alternative methods of preparation of soluble keratin from chicken feathers *Waste Biomass Valorization* **8** 1043–8
[66] Hansen S 2012 BayesApp: a web site for indirect transformation of small-angle scattering data *J. Appl. Crystallogr.* **45** 566–7
[67] Breßler I, Kohlbrecher J and Thünemann A F 2015 SASfit: a tool for small-angle scattering data analysis using a library of analytical expressions *J. Appl. Crystallogr.* **48** 1587–98
[68] Barsoukov E and Ross Macdonald J 2005 *Impedance Spectroscopy: Theory, Experiment, and Applications* ed E Barsoukov and J R Macdonald 2nd edn (Wiley)
[69] David M, Feldman Y and Ishai P B 2023 Dielectric spectroscopy and techniques *Non-Destructive Material Characterization Methods* (Elsevier) pp 587–619
[70] Trukhan E M 1963 *Sov. Phys. Solid State* **4** 25601
[71] Wubbenhorst M and Van Turnhout J 2002 Analysis of complex dielectric spectra. I. One-dimensional derivative techniques and three-dimensional modelling *J. Non-Cryst. Solids.* **305** 40–49
[72] Steeman P A M and Van Turnhout1 J 1994 Fine structure in the parameters of dielectric and viscoelastic relaxations *Macromolecules* **27** 5421–7
[73] Cole H S and Davidson D W 1951 Dielectric relaxation in glycerol, propylene glycol *J. Chem. Phys.* **19** 1484–90
[74] Cole K S and Cole R H 1941 Dispersiona and absorption in dielectrics: I. Alternating CUrrent characteristics *J. Chem. Phys.* **9** 98–105
[75] Cole K S and Cole R H 1942 Dispersion and absorption in dielectrics: II. Direct current characteristics *J. Chem. Phys.* **10** 98–105
[76] Havriliak S and Negami S 1966 A complex plane analysis of α-dispersions in some polymer systems *J. Polym. Sci.* **14** 99–117
[77] Matos B R, Santiago E I, Rey J F Q and Fonseca F C 2014 Origin of α and β relaxations of Nafion *Phys. Rev.* E **89** 052601
[78] Guo L, Li W, Gu Z, Wang L, Guo L, Ma S, Li C, Sun J, Han B and Chang J 2023 Recent advances and progress on melanin: from source to application *Int. J. Mol. Sci.* **24** 4360
[79] Bordi F, Cametti C and Colby R H 2004 Dielectric spectroscopy and conductivity of polyelectrolyte solutions *J. Phys.* **16** R1423–63
[80] Matos B R, Politano R, Rey J F Q, Hermida-Merino D, Schade U, Puskar L and Fonseca F C 2018 Interplay of α/β-relaxation dynamics and the shape of ionomer building blocks *Sci. Rep.* **8** 13441
[81] Matos B R, Santiago E I, Rey J F Q, Scuracchio C H, Mantovani G L, Hirano L A and Fonseca F C 2015 Dc Proton conductivity at low-frequency in Nafion conductivity spectrum probed by time-resolved SAXS measurements and impedance spectroscopy *J. Polym. Sci.* B **53** 822–8
[82] Tierney N K and Register R A 2002 Ion hopping in ethylene-methacrylic acid ionomer melts as probed by rheometry and cation diffusion measurements *Macromolecules* **35** 2358–64
[83] Bedran Z V, Zhukov S S, Abramov P A, Tyurenkov I O, Gorshunov B P, Mostert B and Motovilov K A 2021 Water-activated semiquinone formation and carboxylic

acid dissociation in melanin revealed by infrared spectroscopy *Polymers* **13** 4403
[84] Bridelli M G and Crippa P R 2010 Infrared and water sorption studies of the hydration structure and mechanism in natural and synthetic melanin *J. Phys. Chem.* B **114** 9381–90
[85] Bridelli M G, Tampellini D and Zecca L 1999 The structure of neuromelanin and its iron binding site studied by infrared spectroscopy *Febs Lett.* **457** 18–22
[86] Hyogo R, Nakamura A, Okuda H, Wakamatsu K, Ito S and Sota T 2011 Mid-infrared vibrational spectroscopic characterization of 5,6-dihydroxyindole and eumelanin derived from it *Chem. Phys. Lett.* **517** 211–6
[87] Bilińska B 1996 Progress of infrared investigations of melanin structures *Spectrochim. Acta* A **52** 1157–62
[88] Pralea I E *et al* 2019 From extraction to advanced analytical methods: the challenges of melanin analysis *Int. J. Mol. Sci.* **20** 3943
[89] Fu X, Xie M, Lu M, Shi L, Shi T and Yu M 2022 Characterization of the physicochemical properties, antioxidant activity, and antiproliferative activity of natural melanin from S. reiliana *Sci. Rep.* **12** 2110
[90] Skieresz-Szewczyk K, Jackowiak H, Buchwald T and Szybowicz M 2017 Localization of Alpha-Keratin and Beta-Keratin (Corneous Beta Protein) in the Epithelium on the Ventral Surface of the Lingual Apex and Its Lingual Nail in the domestic goose (Anser Anser f. domestica) by using immunohistochemistry and raman microspectroscopy analysis *Anat. Rec.* **300** 1361–8
[91] Wang X, Shi Z, Zhao Q and Yun Y 2021 Study on the structure and properties of biofunctional keratin from rabbit hair *Materials* **14** 379
[92] Du W, Zhang L, Zhang C, Cao J, Wang D, Li H, Li W and Zeng J 2022 Green and highly efficient wool keratin extraction by microwave induction method *Front. Mater.* **8** 789081
[93] Sharma S, Gupta A, Kumar A, Gek C, Hesam K, Syed K and Saufi M 2018 An efficient conversion of waste feather keratin into ecofriendly bioplastic film *Clean Technol. Environ. Policy* **20** 2157–67
[94] Pabisch S, Puchegger S, Kirchner H O K, Weiss I M and Peterlik H 2010 Keratin homogeneity in the tail feathers of Pavo cristatus and Pavo cristatus mut. alba *J. Struct. Biol.* **172** 270–5
[95] Cheng J, Moss S C and Eisner M 1994 x-ray characterization of melanins—II *Pigment Cell Res.* **7** 263–73
[96] Cheng J, C M S and M E 1994 1994 x-ray characterization of melanins—I *Pigment Cell Melanoma Res.* **7** 255–62
[97] Abramov P A, Ivankov O I, Mostert A B and Motovilov K A 2023 Signatures of pancake bonding in hydrated eumelanin *Phys. Chem. Chem. Phys.* **25** 16212–6
[98] Gallas J M, Littrell K C, SeifertSZajac G W and Thiyagarajan P 1999 Solution structure of copper ion-induced molecular aggregates of tyrosine melanin *Biophys. J.* **77** 1135–42
[99] Littrell K C, Gallas J M, Zajac G W and Thiyagarajan P 2007 Structural studies of bleached melanin by synchrotron small-angle x-ray scattering *Photochem. Photobiol.* **77** 115–20
[100] Wang Y, Sun C N, Fan F, Sangoro J R, Berman M B, Greenbaum S G, Zawodzinski T A and Sokolov A P 2013 Examination of methods to determine free-ion diffusivity and number density from analysis of electrode polarization *Phys. Rev.* E **87** 042308
[101] Awasthi P and Das S 2019 Reduced electrode polarization at electrode and analyte interface in impedance spectroscopy using carbon paste and paper *Rev. Sci. Instrum.* **90** 124103
[102] Gebbie M A *et al* 2017 Long range electrostatic forces in ionic liquids *Chem. Commun.* **53** 1214–24
[103] Palmer L S, Cunliffe A and Hough J M 1952 Dielelectric constant of water film *Nature* **170** 796
[104] Pal P and Ghosh A 2020 Broadband dielectric spectroscopy of BMPTFSI ionic liquid doped solid-state polymer electrolytes: coupled ion transport and dielectric relaxation mechanism *J. Appl. Phys.* **128** 84104
[105] Pal P and Ghosh A 2019 Ion conduction and relaxation mechanism in ionogels embedded with imidazolium based ionic liquids *J. Appl. Phys.* **126** 84104
[106] Dyre J C 2005 A model for the generic alpha relaxation of viscous liquids *Europhys. Lett.* **71** 646–50
[107] Yuan W L, Yang X, He L, Xue Y, Qin S and Tao G H 2018 Viscosity, conductivity, and electrochemical property of dicyanamide ionic liquids *Front. Chem.* **6** 59
[108] Ghiani S, Baroni S, Burgio D, Digilio G, Fukuhara M, Martino P, Monda K, Nervi C, Kiyomine A and Aime S 2008 Characterization of human hair melanin and its degradation products by means of magnetic resonance techniques *Magn. Reson. Chem.* **46** 471–9
[109] Mostert A B *et al* 2024 Exploring the chemistry and composition of black soldier fly eumelanin, a material for a circular economy *Mater. Adv.* **5** 8986–99
[110] Ambrico M, Guazzelli L, Mezzetta A, Cariola A, Valgimigli L, Ambrico P F and Manini P 2024 Entangling imidazolium-based ionic liquids and melanins: a crossover study on chemical vs electronic properties and carrier transport mechanisms *J. Mol. Liq.* **403** 124892
[111] Latypova L, Puzenko A, Levy E and Feldman Y 2020 Dielectric spectra broadening as a signature for dipole-matrix interactions. V. Water in protein solutions *J. Chem. Phys.* **153** 045102
[112] Fan F and Roos Y H 2017 Glass transition-associated structural relaxations and applications of relaxation times in amorphous food solids: a review *Food Eng. Rev.* **9** 257–70
[113] Kobayashi K, Pagot G, Vezzù K, Bertasi F, Di Noto V and Tominaga Y 2021 Effect of plasticizer on the ion-conductive and dielectric behavior of poly (ethylene carbonate)-based Li electrolytes *Polym. J.* **53** 149–55